

1 **Think zinc: Role of zinc poisoning in the intraphagosomal killing of bacteria by**  
2 **the amoeba *Dictyostelium***

3

4 Caroline Barisch<sup>1\*</sup>, Vera Kalinina<sup>1,2</sup>, Louise H. Lefrançois<sup>1</sup>, Joddy Appiah<sup>1</sup>, and Thierry Soldati<sup>1</sup>

5

6 <sup>1</sup>Department of Biochemistry, Faculty of Science, University of Geneva, 30 quai Ernest-Ansermet, Science  
7 II, 1211 Geneva-4, Switzerland

8 <sup>2</sup> present address: Institute of Cytology, Russian Academy of Sciences, Tikhoretsky ave. 4, 194064 St.  
9 Petersburg, Russia

10

11

12

13

14

15

16

17

18

19

20 Running title: Role of Zn and Zn Transporters in *Dictyostelium*

21

22

23

24 \*Corresponding author

25 Caroline.Barisch@unige.ch

26 Tel: +41-22-379-6488

27 Fax: +41-22-379-3499

## 28 **Summary statement**

29 Metal poisoning is one of the bactericidal strategies of macrophages. Here, we describe the dynamics of free  
30 Zn and the role of Zn transporters during phagocytosis in *Dictyostelium*.

## 31 **Abstract**

32 Professional phagocytes have developed an extensive repertoire of autonomous immunity strategies  
33 to ensure killing of bacteria. Besides phagosome acidification and the generation of reactive oxygen species,  
34 deprivation of nutrients and the luminal accumulation of toxic metals are essential to kill ingested bacteria or  
35 inhibit growth of intracellular pathogens. We use the soil amoeba *Dictyostelium discoideum*, a professional  
36 phagocyte that digests bacteria for nutritional purposes, to decipher the role of zinc poisoning during  
37 phagocytosis of non-pathogenic bacteria and visualize the temporal and spatial dynamics of  
38 compartmentalized, free zinc using fluorescent probes. Immediately after particle uptake, zinc is delivered to  
39 phagosomes by fusion with “zincosomes” of endosomal origin, but also by the action of one or more zinc  
40 transporters. We localize the four *Dictyostelium* ZnT transporters to endosomes, the contractile vacuole and  
41 the Golgi apparatus, and study the impact of *znt* knockouts on zinc homeostasis. Finally, we show that zinc is  
42 delivered into the lumen of *Mycobacterium smegmatis*-containing vacuoles, and that *Escherichia coli*  
43 deficient in the zinc efflux P<sub>1B</sub>-type ATPase ZntA is killed faster than wild type bacteria.

## 44 **Keywords**

45 *Dictyostelium*, zinc transporter, zinc poisoning, bacteria killing, phagocytosis

## 46 Introduction

47 Transition metals such as iron (Fe), zinc (Zn), manganese (Mn), cobalt (Co) and copper (Cu) are  
48 essential for the survival of all living organisms [reviewed in (Weiss and Carver, 2018)]. These metals are  
49 incorporated into active sites of metalloenzymes, and organise secondary structures such as Zn finger  
50 domains of many proteins including transcription factors. They are therefore implicated in a wide range of  
51 crucial biological processes. However, excess of these metals is toxic for living organisms, partially because  
52 they compete for metal-binding sites in enzymes. In this context, recent studies have revealed transition  
53 metals as a “double edge sword” during infection of phagocytic cells. Upon phagocytosis, the innate immune  
54 phagocyte restricts intravacuolar bacterial growth either by depleting essential metal ions (e.g. Fe<sup>2+</sup> and  
55 Mn<sup>2+</sup>) or by accumulating others, such as Cu<sup>2+</sup> and Zn<sup>2+</sup>, to intoxicating concentrations [reviewed in  
56 (Flannagan et al., 2015; Lopez and Skaar, 2018)]. On the pathogen side, bacteria have evolved several  
57 strategies to survive excess of metal ions, both in the environment (Ducret et al., 2016; Gonzalez et al., 2018)  
58 and in contact with phagocytes (Botella et al., 2011). For instance, metal efflux transporters such as cation  
59 diffusion facilitators (CDFs) and P-type ATPases remove excess ions from the bacterial cytoplasm (Chan et  
60 al., 2010; Kolaj-Robin et al., 2015).

61 Recently, Zn poisoning was shown to belong to the killing strategies of macrophages (Botella et al.,  
62 2011). Inside macrophages free Zn mainly localizes to late endosomes and lysosomes, and to a smaller  
63 extent to early endosomes (Botella et al., 2011). Zn presumably enters cytoplasmic organelles either by  
64 fusion with Zn-containing endosomes, called zincosomes, or by the direct action of one or several Zn  
65 transporters located at the membrane of the organelle. For example, Zn has been observed to accumulate in  
66 phagolysosomes containing the non-pathogenic bacteria *Escherichia coli*, contributing to their killing. In  
67 addition, Zn transporters are upregulated in macrophages infected with *Mycobacterium tuberculosis* (*Mtb*)  
68 and, after a cytosolic burst, free Zn is delivered and accumulates into the *Mycobacterium*-containing vacuole  
69 (MCV) 24 hours after infection (Botella et al., 2011; Pyle et al., 2017; Wagner et al., 2005). Interestingly,  
70 vice versa, the expression of the P<sub>1</sub>-type Zn exporting ATPase CtpC of *Mtb*, the Zn exporting P<sub>1B</sub>-type  
71 ATPase ZntA of *E. coli* and *Salmonella enterica* serovar Typhimurium, and the Zn Cation Diffusion  
72 Facilitator of *Streptococcus pyogenes* increase during infection of human macrophages and neutrophils  
73 (Botella et al., 2011; Kapetanovic et al., 2016; Ong et al., 2014).

74           However, the import mechanism and the temporal dynamics of Zn inside phagosomes containing  
75 non-virulent and virulent bacteria are still poorly understood. Two families of Zn transporters, ZnT (Zn  
76 transporter Slc30a) and ZIP (Zrt/Irt-like protein Slc39a), have been described in metazoans and in the  
77 amoeba *Dictyostelium discoideum* (hereafter referred to as *Dictyostelium*) [reviewed in (Dunn et al., 2017;  
78 Kambe et al., 2015)]. In metazoans, the ZnT family consists of nine proteins (i.e. ZnT1-8 and ZnT10) that  
79 decrease cytosolic Zn levels by exporting it to the extracellular space or sequestering it into the lumen of  
80 organelles. In contrast, the fourteen members of the ZIP family (i.e. ZIP1-14) catalyse the transport of free  
81 Zn from the extracellular space and organelles into the cytosol [reviewed in (Kambe et al., 2015)]. In  
82 *Dictyostelium*, four putative ZnT proteins and seven ZIP transporters have been identified, but the  
83 directionality of transport has not been experimentally confirmed yet (Dunn et al., 2017; Sunaga et al.,  
84 2008).

85           In recent years, *Dictyostelium* has evolved as a powerful model system to study phagocytosis and  
86 host-pathogen interactions, including cell autonomous defences and bacterial killing [reviewed in (Bozzaro  
87 et al., 2008; Dunn et al., 2017)]. The core machinery of the phagocytic pathway is highly conserved between  
88 human phagocytes and *Dictyostelium*, which digests and kills non-pathogenic bacteria for nutrition. First,  
89 bacteria are recognized by receptors at the plasma membrane, leading to an actin-dependent deformation of  
90 the membrane and the closure of the phagocytic cup (Neuhaus et al., 2002). Few minutes after uptake,  
91 lysosomes fuse with the phagosome, delivering the vacuolar H<sup>+</sup>-ATPase (vATPase), which acidifies the  
92 phagosomal lumen (pH < 4) and contributes to the digestion of bacterial components in concert with various  
93 sets of lysosomal enzymes that are transferred to the phagosome by fusion with endosomes and lysosomes  
94 (Gotthardt et al., 2002). These enzymes are then retrieved from the phagosomes together with the vATPase  
95 starting 45 min after uptake, leading to a post-lysosomal compartment with neutral luminal pH (Gotthardt et  
96 al., 2002). Undigested material is then expelled from the cell by exocytosis. In *Dictyostelium*, free Zn has  
97 been recently localized in the contractile vacuole (CV), an organelle crucial for osmoregulation, and in the  
98 endo-lysosomal system, including phagosomes containing non-pathogenic *E. coli* (Buracco et al., 2017).

99           Here, we monitor free Zn in the endo-phagocytic pathways of *Dictyostelium*, to compare to  
100 knowledge acquired in macrophages, and to understand the evolutionary origin of the metal poisoning  
101 strategy. Moreover, so far it remains unclear whether ZnTs are involved in the Zn accumulation in the  
102 endosomal-lysosomal pathway and consequently we extended our analysis to various *znt* knockouts.

## 103 **Results**

### 104 **In *Dictyostelium*, zincosomes are mainly of lysosomal and post-lysosomal nature**

105 To decipher in more detail the recently reported subcellular localization of free Zn in *Dictyostelium*  
106 (Buracco et al., 2017), cells were pre-incubated overnight with the fluid phase tracer TRITC-dextran, which  
107 accumulates in all endosomes and lysosomes (Hacker et al., 1997), stained with either Fluozin-3 AM (FZ-3,  
108 Fig. 1A) or N1-(7-Nitro-2,1,3-benzoxadiazol-4-yl)-N1,N2,N2-tris(2-pyridinylmethyl)-1,2-ethane-diamine  
109 (NBD-TPEA, Fig. 1B), two fluorescent probes selective for Zn, and fed with 3 µm latex beads. Importantly,  
110 using these two fluorescent probes we were able to localize Zn inside the different cellular compartments,  
111 but not in the cytosol.

112 As revealed by FZ-3 and NBD-TPEA staining (Fig. 1A,B), Zn was clearly detectable inside the  
113 bead-containing phagosome (BCP, asterisk) and zincosomes, that colocalised with the endosomal marker  
114 TRITC-dextran (arrowheads). To define more precisely the identity of zincosomes, *Dictyostelium* expressing  
115 VatB-RFP, a marker of lysosomes and the contractile vacuole (Bracco et al., 1997), or RFP-VacA, a marker  
116 of post-lysosomes (Wienke et al., 2006), were stained with both Zn-probes and fed with latex beads (Fig.  
117 1C-G). Using these markers Zn was detected inside bladders of the CV before discharge (Fig. 1C, arrows,  
118 Movie 1), in VatB-RFP-positive lysosomes (Fig. 1E, arrowheads) and in VatB-RFP-negative but RFP-  
119 VacA-positive post-lysosomes (Fig. 1D,F,G; arrowheads). Besides the osmoregulatory function of the CV  
120 and its role in Ca<sup>2+</sup> sequestration, it is proposed to serve as a transient sink for divalent metals (Bozzaro et  
121 al., 2013). Consequently, our observations are in line with the hypothesis that toxic metals and other ions are  
122 expelled from the cell via the CV (Bozzaro et al., 2013; Heuser et al., 1993). Importantly, we observed that  
123 lysosomes were never labelled by FZ-3 (Fig. 1D, Movie 1), whereas NBD-TPEA never fluoresced inside the  
124 CV and post-lysosomes.

125 Taken together, our data support the localization of Zn inside zincosomes that are of lysosomal and  
126 post-lysosomal nature, as well as inside BCPs and in the CV (Fig. 1H).

### 127 **Localization of free Zn during phagocytosis in *Dictyostelium***

128 We precisely monitored the dynamics of appearance and accumulation of Zn in the BCP by time-  
129 lapse microscopy (Fig. 2A-D). Strikingly, the NBD-TPEA signal became visible inside BCPs very early  
130 after uptake, peaked at 15-20 min and then disappeared until the beads were exocytosed (Fig. 2A,C; Movie

131 2), while the FZ-3 signal was first observed only after approximately 20 min post-uptake, peaked at 35-40  
132 min and persisted until exocytosis (Fig. 2B,D; Movie 3). We verified that the two probes were specific for  
133 Zn, since the signals of both NBD-TPEA and FZ-3 were eliminated by TPEN [N,N,N',N'-tetrakis-(2-  
134 pyridylmethyl) ethylenediamine], a cell-permeant Zn chelator, but not by the non-permeant Zn chelator  
135 DTPA (diethylenetriaminepentaacetic acid) nor the calcium and magnesium (Mg) cell-impermeant chelator  
136 EDTA (ethylenediaminetetraacetic acid, Fig. S1A-B).

137 It is known that a pH lower than 5 quenches by 50% the FZ-3 signal (Gee et al., 2002). On the  
138 contrary, NBD-TPEA is not affected by low pH, but quenched by  $\text{Cu}^{2+}$  concentrations around 30  $\mu\text{M}$  (Xu et  
139 al., 2009). The phagosomes of *Dictyostelium*, more acidic than those in macrophages (Yates et al., 2005),  
140 reach a  $\text{pH} < 3.5$  a few minutes after particle uptake (Marchetti et al., 2009; Sattler et al., 2013), which could  
141 explain the fact that in wild type cells most of the BCPs became FZ-3- fluorescent only after approximately  
142 30 minutes of bead uptake (Fig. 2C,D). In line with that hypothesis, the BCPs of a *pikfyve* knockout (KO),  
143 inhibited in phagosomal acidification (Buckley et al., 2018), became FZ-3-fluorescent 2 min after uptake,  
144 and remained brightly fluorescent until exocytosis (Fig. 2E). In sharp contrast, the BCPs of the *wash* mutant,  
145 which cannot reneutralize phagosomes due to a defect in the retrieval of the vATPase (Carnell et al., 2011),  
146 did not show any FZ-3-fluorescence (Fig. 2F). These results confirm that FZ-3 is quenched in early BCPs,  
147 due to the low luminal pHs, and becomes fluorescent only during reneutralization, when the vATPase is  
148 retrieved (Fig. 1D). Regarding the sensitivity of NBD-TPEA to Cu, cells were pre-treated with different  
149 concentrations of  $\text{CuSO}_4$  before incubation with the probe and beads. Five  $\mu\text{M}$  of  $\text{CuSO}_4$  was sufficient to  
150 completely quench the signal of NBD-TPEA inside BCPs (Fig. S1C), indicating that its fluorescence is  
151 likely quenched by the import of Cu into maturing BCPs. Altogether, integrating the information acquired  
152 with both dyes (Fig. 1,2, Fig. S1), we conclude that free Zn is in fact present inside BCPs from early stages  
153 after bead uptake and until exocytosis of the particle. In addition, FZ-3 and NBD-TPEA can be used in  
154 combination with fluorescent organelle reporters to decipher the localization and function of Zn during  
155 grazing on bacteria.

## 156 **Zn can be delivered to phagosomes by fusion with endo-lysosomal compartments**

157 In macrophages, Zn can be delivered to phagosomes via fusion with early endosomes (Botella et al.,  
158 2011). We wondered whether this was also the case in *Dictyostelium*. Careful examination of amoebae

159 during the phagocytosis assays mentioned above (i.e. preincubation with TRITC-dextran, staining with FZ-3  
160 or NBD-TPEA and feeding with 3  $\mu$ m latex beads) revealed that zincosomes observed in the vicinity of the  
161 BCP (asteriks) can sometime be captured in the process of fusion with BCPs, during which they deliver their  
162 content into the BCP lumen, leading to a crescent shape that increased and spread over time (Fig. 3A, Movie  
163 4, arrows). These observations suggest that large amounts of Zn are delivered to maturing BCPs via  
164 zincosome-phagosome fusion. Interestingly, a large fraction of the delivering zincosomes were surrounded  
165 by AmtA, an ammonium transporter present in endosomes and phagosomes (Kirsten et al., 2008; Uchikawa  
166 et al., 2011), confirming their endosomal nature (Fig. 3B).

167 On the other hand, it was also observed that Zn, detected with NBD-TPEA, was retrieved from  
168 BCPs (asterisks) by fission leading to the formation of new zincosomes (Fig. 3C, Movie 5, arrows). In  
169 summary, one way to deliver Zn to and retrieve it from phagosomes in *Dictyostelium* is by fusion and fission  
170 events with zincosomes of endosomal origin.

#### 171 **Subcellular localization of ZnTs in *Dictyostelium***

172 Zn is sequestered into cellular organelles by Zn transporters of the ZnT family [reviewed in (Kambe  
173 et al., 2015)]. In order to determine the localization of the *Dictyostelium* ZnT transporters, cells expressing  
174 fluorescent chimeras of each of the four ZnT proteins were fixed and stained with antibodies against several  
175 CV and endosomal markers (Fig. 4 and 5). ZntA-mCherry partially co-localized with VatA, a subunit of the  
176 vATPase present in both lysosomes and membranes of the CV network (Neuhaus et al., 1998), and perfectly  
177 co-localized with Rhesus50, a protein that localizes exclusively to the CV [(Benghezal et al., 2001); Fig.  
178 4A].

179 To monitor whether ZntA-mCherry might additionally localize to phagosomes at some stage of  
180 maturation, cells were fed with latex beads, fixed and stained with an antibody against p80 (Fig. 4B). These  
181 experiments excluded colocalisation of ZntA and p80 (Fig. 4B), and highlighted that ZntA-mCherry was in  
182 fact never detected in BCPs (Fig. S2, asterisks). To confirm the exclusive presence of ZntA at CV  
183 membranes, live microscopy was performed on ZntA-mCherry-expressing cells incubated with FZ-3. The  
184 fluorescent probe accumulated in ZntA-positive bladders of the CV that frequently discharged their content,  
185 expelling FZ-3-chelated Zn to the extracellular milieu (Fig. 4C, arrows). Therefore, we conclude that ZntA is  
186 located exclusively to the CV bladders and network.

187 Using the same approach, cells expressing ZntB-mCherry and incubated with FZ-3 were fed latex  
188 beads, revealing the presence of ZntB-mCherry at BCPs (Fig. 4D asterisks) starting from 6 min to until  
189 35 min after bead uptake (arrows, Movie 6). In addition, ZntB-mCherry was also observed around FZ-3-  
190 positive zincosomes (Fig. 4D, arrowheads). The ZntB-mCherry-labelled zincosomes (Fig. 4E, arrowheads)  
191 and BCPs (Fig. S3A, asterisks) were also positive for NBD-TPEA, indicating that the ZntB-positive  
192 compartments can be acidic and likely contain a relatively low Cu concentration. In addition, ZntB-mCherry  
193 partially co-localized with p80 at BCPs (Fig. 4F,G), indicating their lysosomal or early post-lysosomal  
194 nature. This is in line with the observation that ZntB-mCherry also co-localized with the vATPase (Fig. S3B)  
195 but neither with Rhesus50 nor with the endoplasmic reticulum marker PDI (Fig. S3B). Similar to its human  
196 homolog ZNT10 (Bosomworth et al., 2012; Dunn et al., 2017), ZntB was also located at recycling  
197 endosomes and/or the Golgi apparatus, as determined by its juxtannuclear co-localization with p25 [(Charette  
198 et al., 2006); Fig. 4H]. Note that, in *Dictyostelium*, recycling endosomes concentrate around the Microtubule  
199 Organizing Center (MTOC), a region where typically the Golgi apparatus is also located. These results lead  
200 us to conclude that ZntB localizes mainly to organelles of the endosomal pathway.

201 To decipher the subcellular localization of ZntC and ZntD, homologs of the human ZNT6 and  
202 ZNT7, respectively (Dunn et al., 2017), cells expressing ZntC- and ZntD-mCherry were fixed and stained  
203 with antibodies against p80 and p25, a marker for recycling endosomes. ZntC- and ZntD-mCherry both co-  
204 localized with p25 in the juxtannuclear region (Fig. 5A,B), and did not colocalize significantly with p80 (Fig.  
205 5C,D), suggesting that these transporters either locate in recycling endosomes that are usually low in p80  
206 (Charette et al., 2006), or in the Golgi apparatus. Importantly, ZntC- and ZntD-mCherry were not observed  
207 at BCPs at any stage of maturation (Fig. 5E,F). The locations of the various *Dictyostelium* ZnTs are  
208 schematized in Fig. 5G.

### 209 **ZntA is the main Zn transporter of the CV**

210 Zn accumulates inside the CV and is expelled from the cell when the CV discharges (Fig. 1C, 4C).  
211 Since ZntA was the only ZnT localized at the CV membrane (Fig. 4A-C, Fig. S2), we wondered whether  
212 ZntA was involved in the import of Zn into the CV lumen. To test this hypothesis, a *zntA* KO was created  
213 (see Materials and Methods and Fig. S4A,B), and wild type and *zntA* KO cells expressing VatB-RFP were  
214 incubated with FZ-3 (Fig. 6A,B). To verify that the absence of ZntA did not alter the dynamics of Zn



215 delivery into BCPs, cells were fed with 3  $\mu$ m latex beads during the assay. No difference in FZ-3 signal  
216 intensity nor in Zn delivery to BCPs were observed between wild type and mutant cells (Fig. 6A-B).  
217 However, Zn, which was found in the VatB-RFP-positive CV of wild type cells at all time points (Fig. 6A),  
218 was strikingly absent from the CV of *zntA* KO cells (Fig. 6B). This suggests that ZntA mediates the main  
219 route of Zn delivery into the CV. Overexpressing mCherry-ZntA in *zntA* KO cells rescued the transport of  
220 Zn inside the CV network (Fig. 6C). Interestingly, when cells expressing AmtA-mCherry were stained with  
221 NBD-TPEA, the intensity of the signal in zincosomes of the *zntA* KO was more intense than in wild type  
222 cells (Fig. 6D, E). Importantly, knocking out *zntA* did not alter the number of zincosomes (Fig. 6F).

223 In conclusion, these data indicate that ZntA is the main Zn transporter of the CV system, and that the  
224 absence of ZntA leads to an increased concentration of Zn in the endosomal system (Fig. 6G).

### 225 **ZntB is the main lysosomal and post-lysosomal Zn transporter**

226 As mentioned above, ZntB localized at zincosomes and phagosomes (Fig. 4D-H, Fig. S3). To test  
227 whether ZntB mediates the transport of Zn into these compartments, a *zntB* KO, generated within the  
228 Genome Wide *Dictyostelium* Insertion (GWDI) project, was used (Fig. S4C). The insertion site of the  
229 blasticidin cassette was confirmed by genomic PCR (Fig. S4D). Wild type and *zntB* KO cells were incubated  
230 over night with TRITC-dextran, stained with FZ-3 or NBD-TPEA, and fed with 3  $\mu$ m latex beads (Fig. 7A-  
231 D). Strikingly, the BCPs of *zntB* KO cells appeared to be devoid of both FZ-3 and NBD-TPEA signals (Fig.  
232 7A and D). By adjusting the image settings and by quantification of the integrated signal intensity inside  
233 BCPs, the signal in *zntB* KO cells was shown to be decreased by approximately 60% compared to wild type  
234 (Fig. 7B and C). The residual amount of Zn detected might be delivered to BCPs by fusion with zincosomes  
235 that are also present in the *zntB* KO (Fig. 7D, arrows). Importantly, overexpression of ZntB-mCherry in the  
236 *zntB* KO rescued the defect in Zn content (Fig. 7E).

237 We propose that ZntB is the main Zn transporter in lysosomes and post-lysosomes (Fig. 7F), and that,  
238 in its absence, residual levels of Zn are reached within these compartments by fusion with zincosomes or  
239 trafficking from recycling endosomes, where Zn is transported by ZntC or ZntD.

240 Since ZntB is located at BCPs, a generic type of phagosomes that have a relatively transient nature,  
241 leading to particle exocytosis after about 60 minutes, we wondered whether ZntB is also present at  
242 compartments containing the non-pathogenic mycobacterium *M. smegmatis*, which are documented to have

243 phagolysosomal identity but are more persistent, releasing killed bacteria after a couple of hours. ZntB-  
244 mCherry localized at the membrane of the MCV immediately after bacteria uptake, and Zn, detected by  
245 NBD-TPEA, also accumulated inside the MCV at the same time (Fig. S5). The concentration of  
246 intraphagosomal Zn appeared to increase during the early stages of infection (from 1 to 33 min post-uptake),  
247 which agrees with the hypothesis of ZntB being the main lysosomal Zn transporter. Strikingly, as we  
248 observed before for BCPs (Fig. 7D), Zn could also be delivered to the MCV by fusion of ZntB-mCherry-  
249 decorated zincosomes (Fig. S5, 33 min).

## 250 **Zn poisoning contributes to the killing of phagocytosed bacteria**

251 In macrophages, infection with *E. coli* leads to an increase in the cytosolic level of Zn, followed by  
252 its transport inside phagosomes (Botella et al., 2011). When *Dictyostelium* was infected with *E. coli*, we  
253 could not observe a cytosolic burst of Zn, but Zn appeared in the phagosomes rapidly after uptake (Fig. 8A).  
254 This was due, at least in part, to fusion of the phagosomes with zincosomes (Fig. 8A, arrowheads) in line  
255 with our previous observations (Fig. 3A,S5) and the findings in macrophages (Botella et al., 2011).

256 To determine whether Zn contributes to intraphagosomal bacteria killing by *Dictyostelium*, a Zn-  
257 hypersensitive *E. coli* mutant with an inactivated P<sub>1B</sub>-type Zn efflux ATPase [ $\Delta zntA$ , (Rensing et al., 1997)]  
258 was used. We first confirmed the hypersensitivity of this mutant to Zn (Fig. 8B), since 0.2 mM of Zn was  
259 enough to strongly inhibit its growth *in vitro*, whereas the proliferation of wild type cells was only inhibited  
260 by concentrations of Zn above 1.25 mM (Fig. 8B). This differential and dose-dependent inhibition of  
261 bacteria growth was not observed for other metals such as Cu, Fe or Mn (Fig. S6A-C). In line with  
262 observations in macrophages (Botella et al., 2011), *Dictyostelium* killed the  $\Delta zntA$  mutant bacteria faster than  
263 the wild type *E. coli* (Fig. 8C,D). Interestingly, both *E. coli* strains were killed faster by the *Dictyostelium*  
264 *zntA* KO than by wild type *Dictyostelium* (Fig. 8C), while no significant difference in killing was observed  
265 between *Dictyostelium* wild type and *zntB* KO cells (Fig. 8D). This suggests that accumulation of Zn in the  
266 phagolysosomes contributes to bacterial killing and that these compartments harbour a higher Zn  
267 concentration in the *zntA* KO than in wild type *Dictyostelium*.

## 268 Discussion

269 Intracellular bacteria and pathogens are limited to nutrients that are available inside the host cell.  
270 Professional phagocytes are able to exploit this dependence and have developed strategies to restrict  
271 intracellular bacteria growth or killing. For instance, essential nutrients such as Fe and Zn are either withheld  
272 from the pathogen-containing vacuole or pumped into the phagosomal lumen to ensure bacteria killing in  
273 concert with other immunity factors. Nramp1 mediates Fe sequestration from the phagosome and leads  
274 consequently to the starving of the phagosomal bacteria (Bozzaro et al., 2013; Peracino et al., 2006).  
275 Surprisingly, both nutrient deprivation (Djoko et al., 2015; Kehl-Fie and Skaar, 2010; Subramanian Vignesh  
276 et al., 2013) and metal poisoning have been reported in the case of Zn (Botella et al., 2011; McDevitt et al.,  
277 2011; Soldati and Neyrolles, 2012). Here, we investigated the subcellular localization and role of Zn in  
278 phagocytosis and killing using *Dictyostelium* as a model professional phagocyte.

279 Inside cells Zn is either bound to proteins or sequestered as free zinc into the various cellular  
280 compartments or vesicles. In mammals, 50% of the total cellular Zn is present in the cytoplasm, 30 to 40% is  
281 in the nucleus, and 10% is located at the plasma membrane [reviewed in (Kambe et al., 2015)]. The cytosolic  
282 Zn concentration ranges from picomolar to low nanomolar (Vinkenborg et al., 2009).

283 By using two fluorescent probes, FZ-3 and NBD-TPEA, we investigated the cellular distribution of  
284 compartmentalized free Zn in the professional phagocyte *Dictyostelium*. In line with previous observations  
285 from Buracco and colleagues (Buracco et al., 2017), Zn located inside the endolysosomal system and, more  
286 precisely, inside zincosomes of lysosomal and post-lysosomal nature (Fig. 1E – G and summarizing scheme  
287 Fig. 1H), as well as inside the CV network (Fig. 1C and Fig. 4C). In addition, Zn was present in the lumen of  
288 phagosomes soon after bead uptake and until exocytosis (Fig. 2A-D).

289 The total cellular Zn concentration varies in the range of 10-100 micromolar in mammalian cells  
290 (Krezel and Maret, 2006). It was suggested that the concentration of cytosolic Zn fluctuates in response to  
291 various stimuli (Kambe et al., 2015). For instance, after incubation of macrophages with *E. coli*, Zn is  
292 released from storage complexes, followed by pumping and sequestration into phagosomes. However, this  
293 was not observed in *Dictyostelium* neither by feeding cells with beads nor with bacteria (Fig. 2A, 8A, S5).  
294 We reason that, since the concentration of cytosolic Zn is very low [between pico- and low nanomolar;

295 reviewed (Kambe et al., 2015)], it is consequently under the detection limit of FZ-3 and NBD-TPEA,  
296 explaining why we could not monitor cytosolic Zn.

297 The subcellular homeostasis of Zn is tightly regulated through uptake, storage, re-distribution and efflux  
298 mechanisms that are, among other, mediated by Zn transporters of the ZnT and ZIP family (Bird, 2015).  
299 Seven members of the ZIP family and four members of the ZnT family have been identified in *Dictyostelium*  
300 (Dunn et al., 2017; Sunaga et al., 2008). ZntC and ZntD are the *Dictyostelium* homologs of the human ZnT6  
301 (Huang et al., 2002) and ZnT7 (Kirschke and Huang, 2003), respectively. As their mammalian counterparts  
302 (Kambe et al., 2015), they localized at recycling endosomes and/or in the Golgi apparatus of *Dictyostelium*  
303 (Fig. 5A-F, summarizing scheme Fig. 5G). ZntA, which is not closely related to any specific human Zn  
304 transporter (Dunn et al., 2017), was located at the membrane of the CV (Fig. 4A-C, Fig. S2A, summarizing  
305 scheme Fig. 5G). *Dictyostelium* ZntB is the closest homolog of human ZnT1 and ZnT10 (Dunn et al., 2017).  
306 Whereas ZnT1 is a plasma membrane protein (Palmiter and Findley, 1995), ZnT10 locates at the Golgi  
307 apparatus and at early and/or recycling endosomes (Patrushev et al., 2012), a location similar to the one of  
308 ZntB, described here. (Fig.4H). In addition, ZntB was observed at BCPs at the phagolysosomal stage (Fig.  
309 4D-G; Fig. S3A,B). Loss of ZntB lead to a 60%-reduction of the FZ-3 fluorescence inside BCPs (Fig. 7A-E),  
310 leading to the conclusion that ZntB is the main endo-lysosomal Zn transporter in *Dictyostelium*  
311 (summarizing scheme Fig. 7F).

312 Interestingly, *Dictyostelium* growth was only inhibited by Zn or Cu concentrations at 50- or 500-fold the  
313 physiological levels, suggesting a very efficient control of Zn and Cu homeostasis (Buracco et al., 2017). In  
314 *Dictyostelium* cells, a classical metallothionein activity is not detected (Burlando et al., 2002) and  
315 consequently the CV was proposed to serve as a detoxification system for metal ions such as Fe, Zn and Cu  
316 (Bozzaro et al., 2013; Buracco et al., 2017; Peracino et al., 2013).

317 Changes in the cytosolic Zn levels under non-steady-state conditions are remedied in a process  
318 described as “muffling” by diverse mechanisms such as the cytosolic buffering by metallothioneins, the  
319 extrusion of Zn from the cell, and the sequestration of Zn into organelles (Colvin et al., 2010). In  
320 *Dictyostelium*, Zn is sequestered into the CV thanks to the transport by the ZntA (Fig. 6A,B). Because we  
321 observed an accumulation of Zn within lysosomes in *zntA* KO cells (Fig. 6A-F, summarizing scheme Fig.  
322 6G), we conclude that, in this mutant, Zn is rerouted from the cytosol to lysosomes in order to avoid toxic  
323 levels of cytosolic Zn.

324 Botella and colleagues revealed metal poisoning of ingested microbes as a novel killing strategy of  
325 macrophages (Botella et al., 2011). Besides zinc poisoning one can speculate that bacteria also have to face  
326 Cu poisoning inside the phagosome. In line with that hypothesis, NBD-TPEA was quenched at later  
327 phagocytic stages (Fig. 2A,B and Fig. S1C), a plausible sign of Cu accumulation. Interestingly, the  
328 expression of the *Dictyostelium* homolog of the phagosomal copper transporter ATP7A is upregulated upon  
329 feeding with bacteria, consistent with a possible role of Cu poisoning during phagocytosis (Hao et al., 2016).

330 Excess Zn levels might inhibit bacterial ATP production by impairing the activity of cytochromes  
331 (Beard et al., 1995). Additionally, excess Zn might replace other metals in the active site of various enzymes  
332 or occupy non-specific binding sites (Nies, 1999). Here, we investigated the role of Zn during phagocytosis  
333 and killing of bacteria by *Dictyostelium*. Zn was observed inside phagosomes containing *E. coli* (Fig. 8A)  
334 and *M. smegmatis* (Fig. S5). Similar to the situation described in macrophages, an *E. coli* strain deficient in  
335 the Zn efflux P<sub>1B</sub>-type ATPase ZntA was killed faster than the wild type (Fig. 8C,D), leading to the  
336 conclusion that Zn poisoning belongs to the killing repertoire of *Dictyostelium*. While the accumulation of  
337 Zn inside lysosomes of the *zntA* KO leads to a better killing capacity of *Dictyostelium* (Fig. 8C), bacteria  
338 killing in the *zntB* KO was unaffected (Fig. 8D). This suggests that Zn poisoning is an evolutionarily  
339 conserved process and might act in concert with other killing factors such as phagosomal acidification, ROS  
340 production, and deprivation or poisoning by other metals, which would compensate for the loss of ZntB.

## 341 **Materials and Methods**

### 342 *Dictyostelium* plasmids, strains and cell culture

343 All the *Dictyostelium* material used for this article is listed below (Table 1). *Dictyostelium* Ax2(Ka)  
344 and AX4 cells were cultured axenically at 22°C in HL5-C medium (Foremedium) supplemented with  
345 100 U/mL penicillin and 100 µg/mL streptomycin to avoid contamination. Cell lines expressing fluorescent  
346 reporters and KO cell lines were cultured in the presence of selective antibiotics [hygromycin (50 µg/ml),  
347 neomycin (5 µg/ml) or blasticidin (5 µg/ml)]. To monitor the localization of ZnTs, *Dictyostelium* was  
348 transformed with plasmids carrying the ZntA-, ZntB-, ZntC- or ZntD-mCherry constructs [pDM1044  
349 backbone (Veltman et al., 2009)]. The *zntA* KO was generated in the Ax2(Ka) background by homologous  
350 recombination following the one-step cloning protocol previously described (Wiegand et al., 2011). In brief,  
351 left and right arms of *zntA* were amplified using the primers 5'-AGCGCGTCTCCAATGCTGCAGGGAAGT  
352 GAGGGTGTG (forward) and 5'-AGCGCGTCTCCGTTGGTTTATGTTTCGTGTTTCATG (reverse) and 5'-  
353 AGCGCGTCTCCCTTCCAACAATAGATCCCGAAG (forward) and 5'-AGCGCGTCTCCTCCCCTGCAG  
354 GTGGATGTGCACTTC-5' (reverse), and cloned into the StarGate® Acceptor Vector pKOS-IBA-Dicty1  
355 using the StarGate cloning kit. The resulting plasmid was transformed into *Dictyostelium* by electroporation,  
356 and positive clones were selected with blasticidin (Fig. S4A). Correct integration into the genome was tested  
357 by PCR using different combinations of primers: *zntA* flanking forward 5'-  
358 CGATTTGTTGTTACCTAAATATTCGTG and *zntA* flanking reverse 5'-CACCCAATTTACTAGTTTC  
359 ACC, *zntA* inside forward 5'-GTGGTGAAGATGGTAGTAGTAGTG and *zntA* inside reverse 5'-CATGA  
360 GTACACCTAAACTTTCACG, Bsr forward 5-AGATCTTGTGAGAAATGTAAATTGATC and Bsr  
361 reverse 5'-TTGAAGAAGTCACTTCCACTCAAATATAC (Fig. S4B).

### 362 *Verification of the zntB REMI KO*

363 The *zntB* KO (AX4 background) was obtained as part of the Genome Wide *Dictyostelium* Insertion  
364 (GWDI) Project (<https://remi-seq.org/>) and was generously provided by Prof Christopher Thompson. The  
365 individual mutant was obtained from the grid. To confirm the insertion site of the blasticidin cassette into the  
366 *zntB* gene, gDNA was isolated from wild type and *zntB* KO using the High Pure PCR Template Preparation  
367 Kit (Roche) and a diagnostic PCR was performed according to the recommendations on the GWDI website.  
368 Primer combinations with the two *zntB* specific primers *zntB* forward 5'- GGCAATTCCACGTTTCATCAG

369 and *zntB* reverse 5'- GTAACGAATT GAATCCAAATCG binding approximately 400 bp up- or downstream  
370 the insertion sides and the two primers specific for the blasticidin cassette pGWDI1 5'-  
371 GTTGAGAAATGTAAATTGATCC and pGWDI2 5'-AT AGAAATGAATGGCAAGTTAG were used to  
372 confirm the insertion.

### 373 *E. coli* and *M. smegmatis* strains and culture

374 *E. coli* wild type and  $\Delta zntA$  were kindly provided by Prof Christopher Rensing [(Rensing et al.,  
375 1997); Chinese Academy of Sciences Beijing (China)], and cultured in LB medium. *M. smegmatis*  
376 (Hagedorn and Soldati, 2007) was cultured in 7H9 medium supplemented with 10% OADC, 0.05%  
377 Tween80 and 0.2% glycerol at 32°C in shaking. Erlenmeyer flasks containing 5 mm glass beads were used  
378 to minimize clumping of bacteria. Vybrant DyeCycle Ruby Stain (Thermo Fisher Scientific) was used to  
379 stain intracellular *M. smegmatis* before live imaging was performed.

### 380 *Imaging of free Zn in Dictyostelium*

381 The day before imaging, *Dictyostelium* was plated on 2- or 4-well ibidi dishes. Three hours before  
382 imaging, HL5-C was changed to SIH [Formedium, full synthetic medium with low Zn concentration (2.3  
383 mg/l ZnSO<sub>4</sub>). After 2 hrs in SIH, cells were washed thrice in Soerensen buffer and stained with 2 μM FZ-3  
384 [Thermo Fisher Scientific (#F-24195), 400 μM stock in DMSO] or 2.5 μg/ml NBD-TPEA [Sigma (#N1040),  
385 0.5 mg/ml stock in DMSO] for 30 min in the dark. In order to synchronize phagocytosis, cells were cooled  
386 on a cold metal plate for 10 min before adding the 3 μm latex-beads [Sigma-Aldrich (#LB30)]. Beads were  
387 mixed with Soerensen buffer and added to the cells. After centrifugation at 500g for 2 min at 4°C, the  
388 medium was carefully aspirated from the dish and an agarose overlay was placed on top of the cells, as  
389 described before (Barisch et al., 2015). Cells were imaged on an inverted 3i Marianas spinning disc confocal  
390 microscope using the 63 × glycerol or 100 × oil objectives. Where indicated, cells were treated for 3 hrs with  
391 different chelators: TPEN [Sigma-Aldrich (#87641)], DTPA [Sigma-Aldrich (#D6518)], EDTA [Sigma-  
392 Aldrich (#E6758)] or CuSO<sub>4</sub> × 5 H<sub>2</sub>O [Sigma (#C3036)] before and throughout staining with the Zn probes.  
393 To label all endosomes TRITC-dextran [70 kDa, Sigma (#T1162)] was added overnight (1 mg/ml; stock 10  
394 mg/ml in ddH<sub>2</sub>O) and throughout FZ-3 and NBD-TPEA staining.

395 The temporal and special dynamics of Zn inside BCPs was quantified using ImageJ and the  
396 “CenterOnClick” plugin (Nicolas Roggli, University of Geneva, unpublished) that automatically centers the



397 “clicked” particle of interest in a recalculated image for further visualization and analysis. The integrated  
398 density inside a “donut” that was drawn around the FZ-3 signal was measured using “plot Z-axis profile”.

#### 399 *Antibodies and immunofluorescence*

400 Antibodies against p80 (Ravanel et al., 2001) were purchased from the Geneva antibody platform  
401 (University of Geneva, Switzerland). An anti-RFP-antibody (Chromotek) was used to increase the  
402 fluorescence of mCherry-expressing fusion proteins. As secondary antibodies, goat anti-mouse, anti-rabbit  
403 and anti-rat IgG coupled to Alexa488, Alexa546 (Thermo Fisher Scientific) or CF640R (Biotium) were used.  
404 For immunofluorescence, *Dictyostelium* cells were fixed with cold MeOH or 4% paraformaldehyde (PFA),  
405 as described previously (Hagedorn et al., 2006). Images were recorded with a Zeiss LSM700 confocal  
406 microscope using a  $63 \times 1.4$  NA or a  $100 \times 1.4$  NA oil-immersion objective.

#### 407 *In vitro effects of heavy metals on E. coli growth*

408 *E. coli* wild type and  $\Delta zntA$  were grown in LB medium overnight at 37°C in shaking at 150 rpm.  
409 Bacteria were diluted to an OD<sub>600</sub> of 0.1 and plated in 96-well plates containing LB medium with different  
410 concentrations of heavy metals (i.e. ZnSO<sub>4</sub>, CuSO<sub>4</sub>, FeCl<sub>3</sub>, MnCl<sub>2</sub> from 0.05 to 2.5 mM). The OD<sub>600</sub> was  
411 measured every hour using a 96-well plate reader (SpectraMax i3, Molecular Devices).

#### 412 *Killing of bacteria and involvement of Zn*

413 Intracellular killing of *E. coli* wild type and  $\Delta zntA$  carrying a GFP-harboring plasmid (Valdivia and  
414 Falkow, 1997) was monitored as described previously (Leiba et al., 2017). A 1:10 dilution of overnight *E.*  
415 *coli* cultures was centrifuged for 4 min at 18000g and bacteria were resuspended in 300  $\mu$ l of filtered HL5-C.  
416 10  $\mu$ l of the bacteria suspension were plated on each well of a 4-well ibidi slide and centrifuged for 10 min at  
417 1500 rpm. 300  $\mu$ l of a  $1 \times 10^6$  cells/ml *Dictyostelium* culture in LoFlo (synthetic low-fluorescent medium,  
418 Foremedium) were overlaid on the bacteria, and images were recorded at 22°C with a Leica AF6000 LX  
419 wide field microscope using the 40  $\times$  dry objective and 30 sec intervals. For each phagocytosed bacterium,  
420 the time between phagocytosis and fluorescence extinction (killing) was determined manually using the  
421 ImageJ software, and the probability of bacterial survival was represented as a Kaplan–Meier estimator. The  
422 data of three independent experiments were pooled and statistical comparisons between Kaplan–Meier  
423 curves were calculated using the log-rank test.



424 To monitor the involvement of Zn in the killing of *E. coli*, *Dictyostelium* cells were stained with  
425 NBD-TPEA, as mentioned above, and bacteria were labelled using CF594 succinimidyl ester [SE, Sigma-  
426 Aldrich (#SCJ4600031)]. Briefly, an overnight culture of bacteria was diluted 1:10 in Soerensen buffer and  
427 incubated with 2  $\mu$ l of a 10mM CF594 SE stock solution (in DMSO) for one hour in the dark. After two  
428 washes with Soerensen buffer, bacteria were resuspended in 1 ml of filtered HL5-C. 10  $\mu$ l of the bacteria  
429 suspension were added to the pre-cooled cells on an 8-well ibidi slide and centrifuged onto cells for 1 min at  
430 500g at 4°C. Images were taken with 90 sec intervals at a spinning disc confocal microscope using the 63  $\times$   
431 objective.

## 432 **Acknowledgments**

433 We gratefully acknowledge the imaging platform of the University of Geneva for their expert and friendly  
434 support. We thank the Genome Wide *Dictyostelium* Insertion Project (<https://remi-seq.org/>) for the *zntB*  
435 REMI cell line. We are grateful to Prof Michael Rensing for sharing the  $\Delta zntA$  *E. coli* knockout and Dr Ana  
436 T. López-Jiménez for constructing the RFP-VacA expression vector. We thank especially Dr Elena  
437 Cardenal-Muñoz for careful reading and editing of the manuscript and thoughtful suggestions and Dr Olivier  
438 Schaad for helping with the statistics. We thank Dr Monica Hagedorn and Prof Markus Maniak for giving  
439 comments on the manuscript and Dr Olivier Neyrolles for inspiring the project. The Soldati laboratory is  
440 supported by multiple grants from the Swiss National Science Foundation. Thierry Soldati is a member of  
441 iGE3 ([www.ige3.unige.ch](http://www.ige3.unige.ch)).

## 442 **References**

- 443 **Barisch, C., Lopez-Jimenez, A. T. and Soldati, T.** (2015). Live Imaging of Mycobacterium marinum  
444 Infection in Dictyostelium discoideum. In *Mycobacteria Protocols (Methods Mol Biol)*, vol. 1285 (eds T.  
445 Parish and D. Roberts), pp. 369-85: Humana, NYC.
- 446 **Beard, S. J., Hughes, M. N. and Poole, R. K.** (1995). Inhibition of the cytochrome bd-terminated NADH  
447 oxidase system in Escherichia coli K-12 by divalent metal cations. *FEMS Microbiol Lett* **131**, 205-10.
- 448 **Benghezal, M., Gotthardt, D., Cornillon, S. and Cosson, P.** (2001). Localization of the Rh50-like protein  
449 to the contractile vacuole in Dictyostelium. *Immunogenetics* **52**, 284-8.
- 450 **Bird, A. J.** (2015). Cellular sensing and transport of metal ions: implications in micronutrient homeostasis. *J*  
451 *Nutr Biochem* **26**, 1103-15.
- 452 **Bosomworth, H. J., Thornton, J. K., Coneyworth, L. J., Ford, D. and Valentine, R. A.** (2012). Efflux  
453 function, tissue-specific expression and intracellular trafficking of the Zn transporter ZnT10 indicate roles  
454 in adult Zn homeostasis. *Metallomics* **4**, 771-9.
- 455 **Botella, H., Peyron, P., Levillain, F., Poincloux, R., Poquet, Y., Brandli, I., Wang, C., Tailleux, L.,**  
456 **Tilleul, S., Charriere, G. M. et al.** (2011). Mycobacterial p(1)-type ATPases mediate resistance to zinc  
457 poisoning in human macrophages. *Cell Host Microbe* **10**, 248-59.
- 458 **Bozzaro, S., Bucci, C. and Steinert, M.** (2008). Phagocytosis and host-pathogen interactions in  
459 Dictyostelium with a look at macrophages. *Int Rev Cell Mol Biol* **271**, 253-300.
- 460 **Bozzaro, S., Buracco, S. and Peracino, B.** (2013). Iron metabolism and resistance to infection by invasive  
461 bacteria in the social amoeba Dictyostelium discoideum. *Front Cell Infect Microbiol* **3**, 50.
- 462 **Bracco, E., Peracino, B., Noegel, A. A. and Bozzaro, S.** (1997). Cloning and transcriptional regulation of  
463 the gene encoding the vacuolar/H<sup>+</sup> ATPase B subunit of Dictyostelium discoideum. *FEBS Lett* **419**, 37-  
464 40.
- 465 **Buckley, C. M., Heath, V. L., Gueho, A., Dove, S. K., Michell, R. H., Meier, R., Hilbi, H., Soldati, T.,**  
466 **Insall, R. H. and King, J.** (2018). PIKfyve/Fab1 is required for efficient V-ATPase delivery to  
467 phagosomes, phagosomal killing, and restriction of Legionella infection. *bioRxiv*.

- 468 **Buracco, S., Peracino, B., Andreini, C., Bracco, E. and Bozzaro, S.** (2017). Differential Effects of Iron,  
469 Zinc, and Copper on Dictyostelium discoideum Cell Growth and Resistance to Legionella pneumophila.  
470 *Front Cell Infect Microbiol* **7**, 536.
- 471 **Burlando, B., Evangelisti, V., Dondero, F., Pons, G., Camakaris, J. and Viarengo, A.** (2002).  
472 Occurrence of Cu-ATPase in Dictyostelium: possible role in resistance to copper. *Biochem Biophys Res*  
473 *Commun* **291**, 476-83.
- 474 **Carnell, M., Zech, T., Calaminus, S. D., Ura, S., Hagedorn, M., Johnston, S. A., May, R. C., Soldati, T.,**  
475 **Machesky, L. M. and Insall, R. H.** (2011). Actin polymerization driven by WASH causes V-ATPase  
476 retrieval and vesicle neutralization before exocytosis. *J Cell Biol* **193**, 831-9.
- 477 **Chan, H., Babayan, V., Blyumin, E., Gandhi, C., Hak, K., Harake, D., Kumar, K., Lee, P., Li, T. T.,**  
478 **Liu, H. Y. et al.** (2010). The p-type ATPase superfamily. *J Mol Microbiol Biotechnol* **19**, 5-104.
- 479 **Charette, S. J., Mercanti, V., Letourneur, F., Bennett, N. and Cosson, P.** (2006). A role for adaptor  
480 protein-3 complex in the organization of the endocytic pathway in Dictyostelium. *Traffic* **7**, 1528-38.
- 481 **Colvin, R. A., Holmes, W. R., Fontaine, C. P. and Maret, W.** (2010). Cytosolic zinc buffering and  
482 muffling: their role in intracellular zinc homeostasis. *Metallomics* **2**, 306-17.
- 483 **Djoko, K. Y., Ong, C. L., Walker, M. J. and McEwan, A. G.** (2015). The Role of Copper and Zinc  
484 Toxicity in Innate Immune Defense against Bacterial Pathogens. *J Biol Chem* **290**, 18954-61.
- 485 **Ducret, V., Gonzalez, M. R., Scignari, T. and Perron, K.** (2016). OprD Repression upon Metal  
486 Treatment Requires the RNA Chaperone Hfq in Pseudomonas aeruginosa. *Genes (Basel)* **7**.
- 487 **Dunn, J. D., Bosmani, C., Barisch, C., Raykov, L., Lefrancois, L. H., Cardenal-Munoz, E., Lopez-**  
488 **Jimenez, A. T. and Soldati, T.** (2017). Eat Prey, Live: Dictyostelium discoideum As a Model for Cell-  
489 Autonomous Defenses. *Front Immunol* **8**, 1906.
- 490 **Flannagan, R. S., Heit, B. and Heinrichs, D. E.** (2015). Antimicrobial Mechanisms of Macrophages and  
491 the Immune Evasion Strategies of Staphylococcus aureus. *Pathogens* **4**, 826-68.
- 492 **Gee, K. R., Zhou, Z. L., Qian, W. J. and Kennedy, R.** (2002). Detection and imaging of zinc secretion  
493 from pancreatic beta-cells using a new fluorescent zinc indicator. *J Am Chem Soc* **124**, 776-8.
- 494 **Gonzalez, M. R., Ducret, V., Leoni, S. and Perron, K.** (2018). Pseudomonas aeruginosa zinc homeostasis:  
495 Key issues for an opportunistic pathogen. *Biochim Biophys Acta*.

- 496 **Gotthardt, D., Warnatz, H. J., Henschel, O., Bruckert, F., Schleicher, M. and Soldati, T.** (2002). High-  
497 resolution dissection of phagosome maturation reveals distinct membrane trafficking phases. *Mol Biol*  
498 *Cell* **13**, 3508-20.
- 499 **Hacker, U., Albrecht, R. and Maniak, M.** (1997). Fluid-phase uptake by macropinocytosis in  
500 Dictyostelium. *J Cell Sci* **110** ( Pt 2), 105-12.
- 501 **Hagedorn, M., Neuhaus, E. M. and Soldati, T.** (2006). Optimized fixation and immunofluorescence  
502 staining methods for Dictyostelium cells. *Methods Mol Biol* **346**, 327-38.
- 503 **Hagedorn, M. and Soldati, T.** (2007). Flotillin and RacH modulate the intracellular immunity of  
504 Dictyostelium to Mycobacterium marinum infection. *Cell Microbiol* **9**, 2716-33.
- 505 **Hao, X., Luthje, F., Ronn, R., German, N. A., Li, X., Huang, F., Kisaka, J., Huffman, D., Alwathnani,**  
506 **H. A., Zhu, Y. G. et al.** (2016). A role for copper in protozoan grazing - two billion years selecting for  
507 bacterial copper resistance. *Mol Microbiol* **102**, 628-641.
- 508 **Heuser, J., Zhu, Q. and Clarke, M.** (1993). Proton pumps populate the contractile vacuoles of  
509 Dictyostelium amoebae. *J Cell Biol* **121**, 1311-27.
- 510 **Huang, L., Kirschke, C. P. and Gitschier, J.** (2002). Functional characterization of a novel mammalian  
511 zinc transporter, ZnT6. *J Biol Chem* **277**, 26389-95.
- 512 **Kambe, T., Tsuji, T., Hashimoto, A. and Itsumura, N.** (2015). The Physiological, Biochemical, and  
513 Molecular Roles of Zinc Transporters in Zinc Homeostasis and Metabolism. *Physiol Rev* **95**, 749-84.
- 514 **Kapetanovic, R., Bokil, N. J., Achard, M. E., Ong, C. Y., Peters, K. M., Stocks, C. J., Phan, M. D.,**  
515 **Monteleone, M., Schroder, K., Irvine, K. M. et al.** (2016). Salmonella employs multiple mechanisms to  
516 subvert the TLR-inducible zinc-mediated antimicrobial response of human macrophages. *FASEB J*.
- 517 **Kehl-Fie, T. E. and Skaar, E. P.** (2010). Nutritional immunity beyond iron: a role for manganese and zinc.  
518 *Curr Opin Chem Biol* **14**, 218-24.
- 519 **Kirschke, C. P. and Huang, L.** (2003). ZnT7, a novel mammalian zinc transporter, accumulates zinc in the  
520 Golgi apparatus. *J Biol Chem* **278**, 4096-102.
- 521 **Kirsten, J. H., Xiong, Y., Davis, C. T. and Singleton, C. K.** (2008). Subcellular localization of ammonium  
522 transporters in Dictyostelium discoideum. *BMC Cell Biol* **9**, 71.
- 523 **Kolaj-Robin, O., Russell, D., Hayes, K. A., Pembroke, J. T. and Soulimane, T.** (2015). Cation Diffusion  
524 Facilitator family: Structure and function. *FEBS Lett* **589**, 1283-95.

- 525 **Krezel, A. and Maret, W.** (2006). Zinc-buffering capacity of a eukaryotic cell at physiological pZn. *J Biol*  
526 *Inorg Chem* **11**, 1049-62.
- 527 **Leiba, J., Sabra, A., Bodinier, R., Marchetti, A., Lima, W. C., Melotti, A., Perrin, J., Burdet, F., Pagni,**  
528 **M., Soldati, T. et al.** (2017). Vps13F links bacterial recognition and intracellular killing in  
529 Dictyostelium. *Cell Microbiol.*
- 530 **Lopez, C. A. and Skaar, E. P.** (2018). The Impact of Dietary Transition Metals on Host-Bacterial  
531 Interactions. *Cell Host Microbe* **23**, 737-748.
- 532 **Marchetti, A., Lelong, E. and Cosson, P.** (2009). A measure of endosomal pH by flow cytometry in  
533 Dictyostelium. *BMC Res Notes* **2**, 7.
- 534 **McDevitt, C. A., Ogunniyi, A. D., Valkov, E., Lawrence, M. C., Kobe, B., McEwan, A. G. and Paton, J.**  
535 **C.** (2011). A molecular mechanism for bacterial susceptibility to zinc. *PLoS Pathog* **7**, e1002357.
- 536 **Neuhaus, E. M., Almers, W. and Soldati, T.** (2002). Morphology and dynamics of the endocytic pathway  
537 in Dictyostelium discoideum. *Mol Biol Cell* **13**, 1390-407.
- 538 **Neuhaus, E. M., Horstmann, H., Almers, W., Maniak, M. and Soldati, T.** (1998). Ethane-  
539 freezing/methanol-fixation of cell monolayers: a procedure for improved preservation of structure and  
540 antigenicity for light and electron microscopies. *J Struct Biol* **121**, 326-42.
- 541 **Nies, D. H.** (1999). Microbial heavy-metal resistance. *Appl Microbiol Biotechnol* **51**, 730-50.
- 542 **Ong, C. L., Gillen, C. M., Barnett, T. C., Walker, M. J. and McEwan, A. G.** (2014). An antimicrobial  
543 role for zinc in innate immune defense against group A streptococcus. *J Infect Dis* **209**, 1500-8.
- 544 **Palmiter, R. D. and Findley, S. D.** (1995). Cloning and functional characterization of a mammalian zinc  
545 transporter that confers resistance to zinc. *EMBO J* **14**, 639-49.
- 546 **Patrushev, N., Seidel-Rogol, B. and Salazar, G.** (2012). Angiotensin II requires zinc and downregulation  
547 of the zinc transporters ZnT3 and ZnT10 to induce senescence of vascular smooth muscle cells. *PLoS*  
548 *One* **7**, e33211.
- 549 **Peracino, B., Buracco, S. and Bozzaro, S.** (2013). The Nramp (Slc11) proteins regulate development,  
550 resistance to pathogenic bacteria and iron homeostasis in Dictyostelium discoideum. *J Cell Sci* **126**, 301-  
551 11.

- 552 **Peracino, B., Wagner, C., Balest, A., Balbo, A., Pergolizzi, B., Noegel, A. A., Steinert, M. and Bozzaro,**  
553 **S.** (2006). Function and mechanism of action of Dictyostelium Nramp1 (Slc11a1) in bacterial infection.  
554 *Traffic* **7**, 22-38.
- 555 **Pyle, C. J., Azad, A. K., Papp, A. C., Sadee, W., Knoell, D. L. and Schlesinger, L. S.** (2017). Elemental  
556 Ingredients in the Macrophage Cocktail: Role of ZIP8 in Host Response to Mycobacterium tuberculosis.  
557 *Int J Mol Sci* **18**.
- 558 **Ravanel, K., de Chasse, B., Cornillon, S., Benghezal, M., Zulianello, L., Gebbie, L., Letourneur, F.**  
559 **and Cosson, P.** (2001). Membrane sorting in the endocytic and phagocytic pathway of Dictyostelium  
560 discoideum. *Eur J Cell Biol* **80**, 754-64.
- 561 **Rensing, C., Mitra, B. and Rosen, B. P.** (1997). The zntA gene of Escherichia coli encodes a Zn(II)-  
562 translocating P-type ATPase. *Proc Natl Acad Sci U S A* **94**, 14326-31.
- 563 **Sattler, N., Monroy, R. and Soldati, T.** (2013). Quantitative analysis of phagocytosis and phagosome  
564 maturation. *Methods Mol Biol* **983**, 383-402.
- 565 **Soldati, T. and Neyrolles, O.** (2012). Mycobacteria and the intraphagosomal environment: take it with a  
566 pinch of salt(s)! *Traffic* **13**, 1042-52.
- 567 **Subramanian Vignesh, K., Landero Figueroa, J. A., Porollo, A., Caruso, J. A. and Deepe, G. S., Jr.**  
568 (2013). Granulocyte macrophage-colony stimulating factor induced Zn sequestration enhances  
569 macrophage superoxide and limits intracellular pathogen survival. *Immunity* **39**, 697-710.
- 570 **Sunaga, N., Monna, M., Shimada, N., Tsukamoto, M. and Kawata, T.** (2008). Expression of zinc  
571 transporter family genes in Dictyostelium. *Int J Dev Biol* **52**, 377-81.
- 572 **Uchikawa, T., Yamamoto, A. and Inouye, K.** (2011). Origin and function of the stalk-cell vacuole in  
573 Dictyostelium. *Dev Biol* **352**, 48-57.
- 574 **Valdivia, R. H. and Falkow, S.** (1997). Probing bacterial gene expression within host cells. *Trends*  
575 *Microbiol* **5**, 360-3.
- 576 **Veltman, D. M., Akar, G., Bosgraaf, L. and Van Haastert, P. J.** (2009). A new set of small,  
577 extrachromosomal expression vectors for Dictyostelium discoideum. *Plasmid* **61**, 110-8.
- 578 **Vinkenborg, J. L., Nicolson, T. J., Bellomo, E. A., Koay, M. S., Rutter, G. A. and Merks, M.** (2009).  
579 Genetically encoded FRET sensors to monitor intracellular Zn<sup>2+</sup> homeostasis. *Nat Methods* **6**, 737-40.

- 580 **Wagner, D., Maser, J., Lai, B., Cai, Z., Barry, C. E., 3rd, Honer Zu Bentrup, K., Russell, D. G. and**  
581 **Bermudez, L. E.** (2005). Elemental analysis of Mycobacterium avium-, Mycobacterium tuberculosis-,  
582 and Mycobacterium smegmatis-containing phagosomes indicates pathogen-induced microenvironments  
583 within the host cell's endosomal system. *J Immunol* **174**, 1491-500.
- 584 **Weiss, G. and Carver, P. L.** (2018). Role of divalent metals in infectious disease susceptibility and  
585 outcome. *Clin Microbiol Infect* **24**, 16-23.
- 586 **Wiegand, S., Kruse, J., Gronemann, S. and Hammann, C.** (2011). Efficient generation of gene knockout  
587 plasmids for Dictyostelium discoideum using one-step cloning. *Genomics* **97**, 321-5.
- 588 **Wienke, D., Drengk, A., Schmauch, C., Jenne, N. and Maniak, M.** (2006). Vacuolin, a flotillin/reggie-  
589 related protein from Dictyostelium oligomerizes for endosome association. *Eur J Cell Biol* **85**, 991-1000.
- 590 **Xu, Z., Gunn-Hee, K., Su, J. H., Min, J. J., Chongmok, L., Injae, S. and Yoon, J.** (2009). An NBD-based  
591 colorimetric and fluorescent chemosensor for Zn<sup>2+</sup> and its use for detection of intracellular zinc ions.  
592 *Tetrahedron* **65**, 2307-2312.
- 593 **Yates, R. M., Hermetter, A. and Russell, D. G.** (2005). The kinetics of phagosome maturation as a  
594 function of phagosome/lysosome fusion and acquisition of hydrolytic activity. *Traffic* **6**, 413-20.

## 595 **Figure Legends**

596 **Fig. 1. Zn accumulates inside the CV network and zincosomes. A.-B.** Zn is observed in the endosomal  
597 system. Cells were incubated with TRITC-dextran, stained with FZ-3 (A) or NBD-TPEA (B), and fed with  
598 3  $\mu$ m latex beads. Arrowheads point to zincosomes. **C.** Zinc is removed from the cell when the CV  
599 discharges. Arrows point to the site of Zn discharge from the CV. Shown are snapshots from Movie 1. Scale  
600 bar, 5  $\mu$ m; Zoom 2  $\mu$ m. **D.** FZ-3 fluoresces inside a BCP when the vATPase is retrieved. Scale bar, 10  $\mu$ m.  
601 TL: transmitted light. **E.** Zincosomes have partially lysosomal characteristics. Scale bars, 5  $\mu$ m; Zoom 2  $\mu$ m.  
602 Cells expressing VatB-RFP were stained with FZ-3 (C and D) or NDB-TPEA (E) and fed with beads. **F.**  
603 Zincosomes have partially post-lysosomal characteristics. Scale bars, 5  $\mu$ m; Zoom 2  $\mu$ m. **G.** Zn accumulates  
604 inside BCPs at the post-lysosomal stage. Scale bars, 5  $\mu$ m; Zoom 1  $\mu$ m. RFP-VacA-expressing cells were  
605 used (F and G). **H.** Scheme. Zn accumulates inside the CV network, zincosomes and the BCP in  
606 *Dictyostelium*. Asterisks label BCPs. BCP: Bead-containing phagosome, v: vATPase, CV: contractile  
607 vacuole, Nu: Nucleus, Z: zincosomes. VacA is shown in red.

608 **Fig. 2. Intracellular distribution of Zn during the phagocytic pathway of *Dictyostelium*. A.-D.** After  
609 NBD-TPEA (A) or FZ3 (C) staining, cells were fed with 3  $\mu$ m latex beads. Single beads were followed by  
610 live microscopy from uptake to exocytosis (Movies 2 and 3). Scale bars, 5  $\mu$ m. Relative fluorescence  
611 intensities inside the BCPs were quantified using ImageJ and the "CenteronClick" plugin (B. and D.). Eight  
612 BCPs per fluorescent probe were quantified. **E.** and **F.** *Dictyostelium* wild type and the *pikfyve* (E) or *wash*  
613 (F) KO were stained with FZ-3 and fed with latex beads. Images were taken 32 min after bead addition.  
614 Scale bars, 10  $\mu$ m. Asterisks indicate the BCPs; arrows point to NBD-TPEA- or FZ-3-positive BCPs.

615 **Fig. 3. Fusion and fission dynamics of zincosomes at the BCPs. A.** Cells were incubated with TRITC-  
616 dextran overnight, stained with FZ-3, and fed with 3  $\mu$ m latex beads. Scale bar, 5  $\mu$ m; Zoom 1  $\mu$ m. Shown  
617 are snapshots from time-lapse Movie 4. **B.** Cells expressing AmtA-mCherry were stained with FZ-3 and fed  
618 with beads. Shown are two examples of AmtA-positive zincosomes fusing with BCPs. Scale bar, 5  $\mu$ m  
619 Zoom, 1  $\mu$ m. **C.** Cells were treated as in A, but stained with NBD-TPEA. Scale bar, 3  $\mu$ m; Zoom 1  $\mu$ m.  
620 Shown are snapshots from time-lapse Movie 5. Asterisks mark the BCPs; arrows label the zincosome-  
621 phagosome fusion site (A and B) or the zincosome-phagosome budding site (C).



622 **Fig. 4. Subcellular localization of ZntA and ZntB. A. and B.** ZntA co-localizes with the CV markers  
623 Rhesus50 and VatA, but not with the endosomal protein p80. ZntA-mCherry expressing cells were fixed and  
624 stained with antibodies against Rhesus50 (A and B), VatA (A) and p80 (B). The signal from ZntA-mCherry  
625 was enhanced with an anti-RFP antibody. Nuclei were stained with DAPI. P: post-lysosome, C: tubular  
626 network of the CV, N: nucleus. Asterisks label BCPs. Scale bars, 5  $\mu\text{m}$  (A) and 10  $\mu\text{m}$  (B). **C.** Zn is enriched  
627 at ZntA-labeled CV compartments. ZntA-mCherry expressing cells were stained with FZ-3. Scale bar, 5  $\mu\text{m}$ .  
628 Arrows point to the sites of CV discharge. **D.** ZntB is recruited to the BCP during phagosome maturation.  
629 Shown are images from a time-lapse movie (Movie 6). Scale bar, 15  $\mu\text{m}$ . **E.** ZntB localizes at zincosomes.  
630 Images were taken live. Arrowheads label zincosomes. Scale bar, 2  $\mu\text{m}$ . Cells expressing ZntB-mCherry  
631 were stained with FZ-3 (D) or NBD-TPEA (E) and fed with 3  $\mu\text{m}$  latex beads. Asterisks label the BCP,  
632 arrows point to a ZntB-positive BCP, arrowheads label ZntB-mCherry-positive zincosomes. **F. – H.** ZntB  
633 co-localizes with endosomal markers. ZntB-mCherry expressing cells were fixed and stained with antibodies  
634 against p80 (F and G) and p25 (H). The signal from ZntB-mCherry was enhanced with an anti-RFP  
635 antibody. Nuclei were stained with DAPI. Asterisks label BCPs, the arrow points to a clustering of ZntB-  
636 mCherry at the juxtannuclear region. N: nucleus. Scale bars, 5  $\mu\text{m}$ .

637 **Fig. 5. Subcellular localization of ZntC and ZntD. A. and B.** ZntC-mCherry (A) and ZntD-mCherry (B)  
638 are localized in the juxtannuclear region. **C. and D.** ZntC-mCherry (C) and ZntD-mCherry (D) do not co-  
639 localize with the endosomal marker p80. Cells were fixed and stained with antibodies against p80 and p25.  
640 Nuclei were stained with DAPI. The signal from ZntC- and ZntD-mCherry was enhanced with an anti-RFP  
641 antibody. Asterisks label a BCP, the arrow points to an enrichment of ZntC- or ZntD-mCherry at the  
642 juxtannuclear region. N: nucleus. Scale bars, 5  $\mu\text{m}$ . **E. and F.** ZntC- and ZntD-mCherry do not co-localize  
643 with BCPs. Cells were stained with FZ3 and fed with 3  $\mu\text{m}$  latex beads. Shown are images from time-lapse  
644 movies. Asterisks label BCPs. Scale bars 20  $\mu\text{m}$ , Zoom 15  $\mu\text{m}$ . **G.** Scheme summarizing the subcellular  
645 localization of ZnTs in *Dictyostelium*. BCP: Bead-containing phagosome, A: ZntA, B: ZntB, C: ZntC, D:  
646 ZntD, v: vATPase, CV: contractile vacuole, Nu: Nucleus, Z: zincosomes. VacA is shown in red.

647 **Fig. 6. ZntA is the main Zn transporter of the CV. A. and B.** Zn is absent from the CV network of the  
648 *zntA* KO. Shown are pictures from time-lapse movies taken at 8 min (upper panel) and 50 min (lower panel)  
649 after the experiment was started. Scale bar, 20  $\mu\text{m}$ ; Zoom 10  $\mu\text{m}$ . **C.** Overexpression of mCherry-ZntA

650 rescues the phenotype of the *zntA* KO. Scale bars, 5  $\mu$ m. Wild type (A) and *zntA* KO (B) expressing VatB-  
651 RFP or *zntA* KO cells expressing mCherry-ZntA (C) were fed with 3  $\mu$ m latex beads and stained with FZ3.  
652 The arrows point to CV bladders filled with Zn in the wild type or mCherry-ZntA overexpressor and to  
653 empty CV bladders in the *zntA* KO. Asterisks label BCPs. **D.** Mislocalized Zn is shuttled into acidic  
654 zincosomes in the *zntA* KO. Cells expressing AmtA-mCherry were stained with NBD-TPEA. Images were  
655 taken by live-microscopy. Scale bar, 10  $\mu$ m **E.** Quantification of D. The total integrated density per cell was  
656 quantified using ImageJ. Statistical significance was calculated with an unpaired t-test (\*\*P < 0.01). Bars  
657 represent the mean and SEM of two independent experiments. In both conditions 30 cells were analysed. **F.**  
658 Same than D, but the microscope settings were adjusted to compare the number of zincosomes in wild type  
659 and *zntA* KO. Arrowheads point to zincosomes. Scale bars, 5  $\mu$ m. **G.** Summarizing scheme showing the  
660 mislocalization of Zn in the *zntA* KO. BCP: Bead-containing phagosome, A: ZntA, B: ZntB, C: ZntC, D:  
661 ZntD, v: vATPase, CV: contractile vacuole, Nu: Nucleus, Z: zincosomes. VacA is shown in red.

662 **Fig. 7. ZntB is the main endosomal Zn transporter. A.-D.** Zn is almost absent from BCPs in the *zntB* KO.  
663 **A.** Cells were incubated over night with TRITC-dextran, co-stained with FZ-3 and fed with 3  $\mu$ m latex  
664 beads. Scale bar, 10  $\mu$ m; Zoom 5  $\mu$ m. **B.** Same than A. To show the residual amount of Zn inside the BCP of  
665 the *zntB* KO, the brightness and contrast of the image was adjusted using ImageJ. Scale bar, 5  $\mu$ m. **C.**  
666 Quantification of A. The integrated density inside the BCPs was quantified using ImageJ. Statistical  
667 significance was calculated with an unpaired t-test (\*\*\*\*P < 0.0001). Bars represent the mean and SEM of  
668 three independent experiments. 103 BCPs were analysed for the wild type and 93 for the *zntB* KO. **D.** Cells  
669 expressing AmtA-mCherry were stained with NBD-TPEA and fed with 3  $\mu$ m latex beads. Scale bars, 5  $\mu$ m.  
670 **E.** The phenotype of the *zntB* KO is rescued by overexpression of ZntB-mCherry. *ZntB* KO expressing ZntB-  
671 mCherry were incubated with FZ-3 and fed with 3  $\mu$ m latex beads. Scale bars, 5  $\mu$ m. Arrows point to  
672 zincosomes. Asterisks label BCPs.

673 **Fig. 8. Zn poisoning is a killing strategy of Dictyostelium. A.** Zn accumulates in *E. coli*-containing  
674 phagosomes. Cells were incubated with NBD-TPEA and fed with CF594-labelled bacteria before live-  
675 imaging. Scale bars, 5  $\mu$ m. Arrows point to phagosomes, arrowheads label zincosomes. **B.** An *E. coli*  $\Delta zntA$   
676 mutant is more sensitive to increasing concentration of ZnSO<sub>4</sub> than the wild type. *E. coli* stains were  
677 incubated in LB. ZnSO<sub>4</sub> was added as indicated. The OD<sub>600</sub> was measured with a 96-well plate reader

678 (SpectraMax i3, Molecular Devices). Statistical differences are calculated with a Bonferroni post hoc test  
679 after two-way ANOVA. Significantly different values were indicated by an asterisk (\*  $P < 0.5$ , \*\*  $P < 0.01$ ).  
680 **C.** Bacteria are killed more efficiently by the *Dictyostelium zntA* KO. **D.** Knockout of ZntB does not affect  
681 bacteria killing. *Dictyostelium* was added to wild type and  $\Delta zntA$  *E. coli* immobilised on an imaging slide  
682 with poly-L-Lysine and a time-lapse movie was recorded with 30 sec intervals. For the Kaplan-Meier  
683 survival curves, the data of three independent experiments were combined. Thirty ingested bacteria were  
684 monitored per condition. The statistical significance was calculated with a log-rank test (\*\* $P = 0.0008$ ,  
685 \*\*\*\*  $P < 0.0001$ ).

## 686 Supporting Information

687 **Fig. S1. Control experiments showing the specificity of FZ-3 and NBD-TPEA for Zn and the**  
688 **quenching of NBD-TPEA by Cu. A.-C.** Cells were incubated with the different chelators or  $\text{CuSO}_4$  at the  
689 indicated concentrations for 3 hrs before the staining with FZ-3 and NBD-TPEA was performed. Afterwards  
690 cells were fed with 3  $\mu\text{m}$  and images were taken by live-microscopy. Importantly, the chelators and  $\text{CuSO}_4$   
691 were present throughout the experiment.

692 **Fig. S2. ZntA-mCherry is not present on BCPs. A. and B.** Cells expressing ZntA-mCherry were stained  
693 with FZ-3 and NBD-TPEA and fed with 3  $\mu\text{m}$  latex beads. Images were taken live. Asterisks label BCPs,  
694 arrows point to FZ-3-positive CV-bladders. Scale bars 10  $\mu\text{m}$  (A), 5  $\mu\text{m}$  (B).

695 **Fig. S3. ZntB-mCherry decorates BCPs and does not co-localize with ER- and CV-markers. A.** ZntB is  
696 present at BCPs at the lysosomal maturation stage. Cells expressing ZntB-mCherry were stained with NBD-  
697 TPEA and fed with 3  $\mu\text{m}$  latex beads. Images were taken live. Scale bar, 5  $\mu\text{m}$ . **B.** ZntB-mCherry co-  
698 localizes with the vATPase at BCPs. Scale bar, 10  $\mu\text{m}$ . **C. and D.** ZntB-mCherry does not localize at the ER  
699 and the at the CV. ZntB-mCherry expressing cells were fixed and stained with antibodies against PDI (C)  
700 and Rhesus50 (D). Nuclei were stained with DAPI. Scale bars, 10  $\mu\text{m}$  (C) and 5  $\mu\text{m}$  (D). Asterisks label a  
701 BCPs, C: tubular network of the CV, N: nucleus.

702 **Fig. S4. Generation of a *zntA* KO by homologous recombination and localization of the insertion in the**  
703 ***zntB* KO. A.** Schematic drawing of the *zntA*-encoding gene locus (ORF, blue) flanked by non-coding  
704 segments. For gene disruption, the resistance cassette (BSr, green) was integrated removing a segment in the

705 middle of the gene (between the inside forward/inside reverse primers) using the StarCombinase and the  
706 StarGate cloning kit. The red arrows indicate primers that were used to monitor correct integration. **B.** PCR-  
707 analysis of two *zntA* mutants (#1 and #2) and wild type (#3). Using the flanking forward/BSR reverse or the  
708 flanking reverse/BSR forward primer combinations small products were obtained in both mutants, but not in  
709 the wild type. The inside forward/inside reverse primer combination yielded a small product in the wild type,  
710 but not in the mutants. Experiments were performed using mutant #1. **C.** The restriction-mediated insertion  
711 of the *zntB* KO interrupts the gene approximately in the middle at chromosomal position 5364176  
712 (Chromosome 3). **D.** A diagnostic PCR was performed to confirm the insertion into *zntB* using the primers  
713 indicated in C.

714 **Fig. S5. ZntB-mCherry is localized at the *M. smegmatis*-containing phagosome.** Cells expressing ZntB-  
715 mCherry were stained with NBD-TPEA and fed with *M. smegmatis*. Images were recorded live. Scale bar,  
716 5  $\mu$ m. Arrows label phagosomes, asterisks point to zincosomes.

717 **Fig. S6. The *zntA* *E. coli* KO is not susceptible to increasing concentrations of CuSO<sub>4</sub>, FeCl<sub>2</sub>, MnCl<sub>2</sub>.** *E.*  
718 *coli* strains were incubated in LB. Metals were added as indicated. The OD<sub>600</sub> was measured with the help of  
719 a 96-well plate reader (SpectraMax i3, Molecular Devices). Statistical differences were calculated with a  
720 Bonferroni post hoc test after two-way ANOVA. Significantly different values were indicated by an asterisk  
721 (\* P < 0.5, \*\* P < 0.01).

722 **Movie 1. Zn is expelled from the cells when the CV discharges.** For more information, see Fig. 1C.

723 **Movie 2. Dynamics of Zn in BCPs of NBD-TPEA-labelled cells.** For more information, see Fig. 2A.

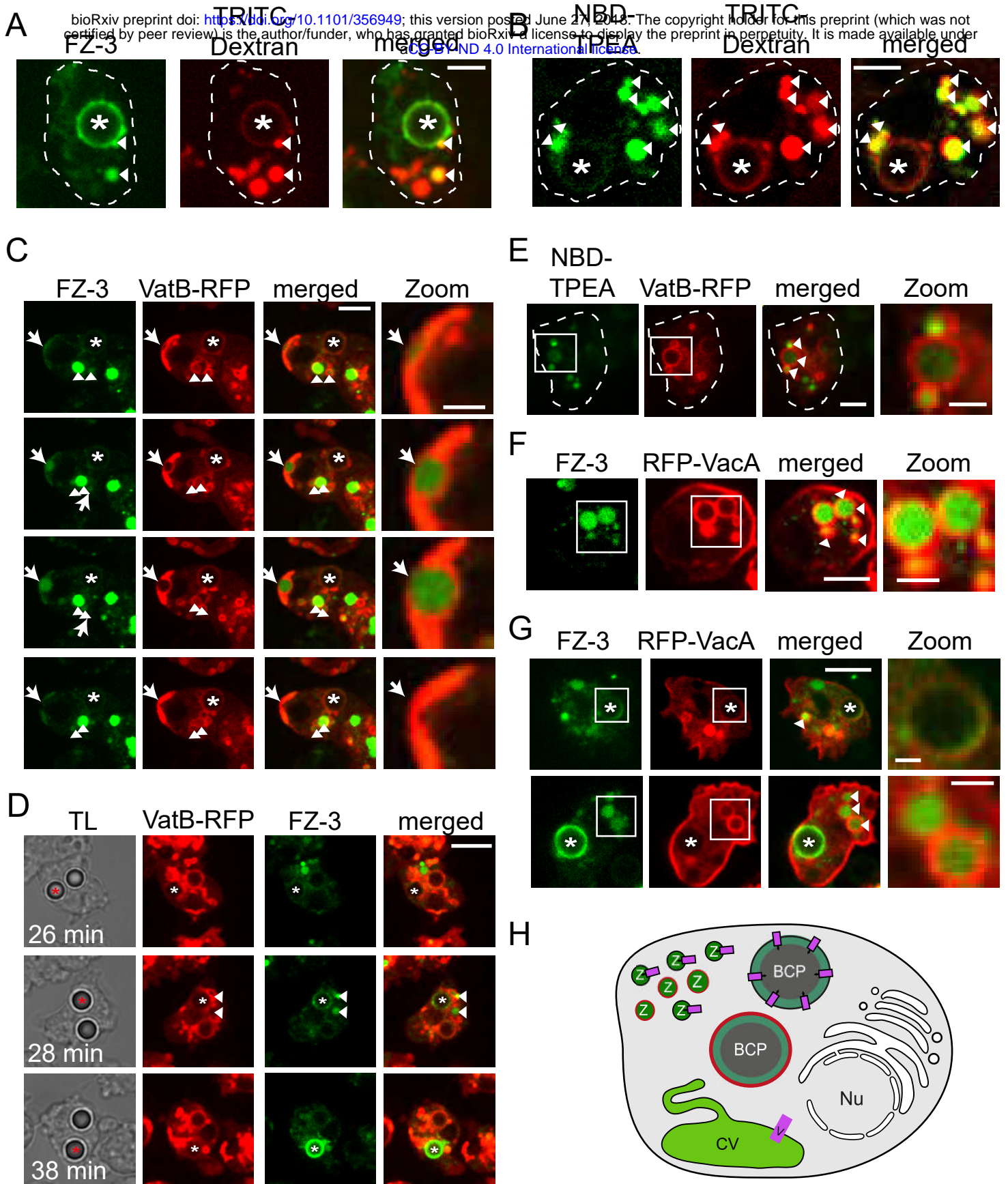
724 **Movie 3. Dynamics of Zn in BCPs of FZ-3-labelled cells.** For more information, see Fig. 2C.

725 **Movie 4. Zincosome-BCP-fusion.** For more information, see Fig. 3A.

726 **Movie 5. Zincosome-BCP-fission.** For more information, see Fig. 3C.

727 **Movie 6. Dynamics of ZntB-mCherry at the BCP.** For more information, see Fig. 4D.

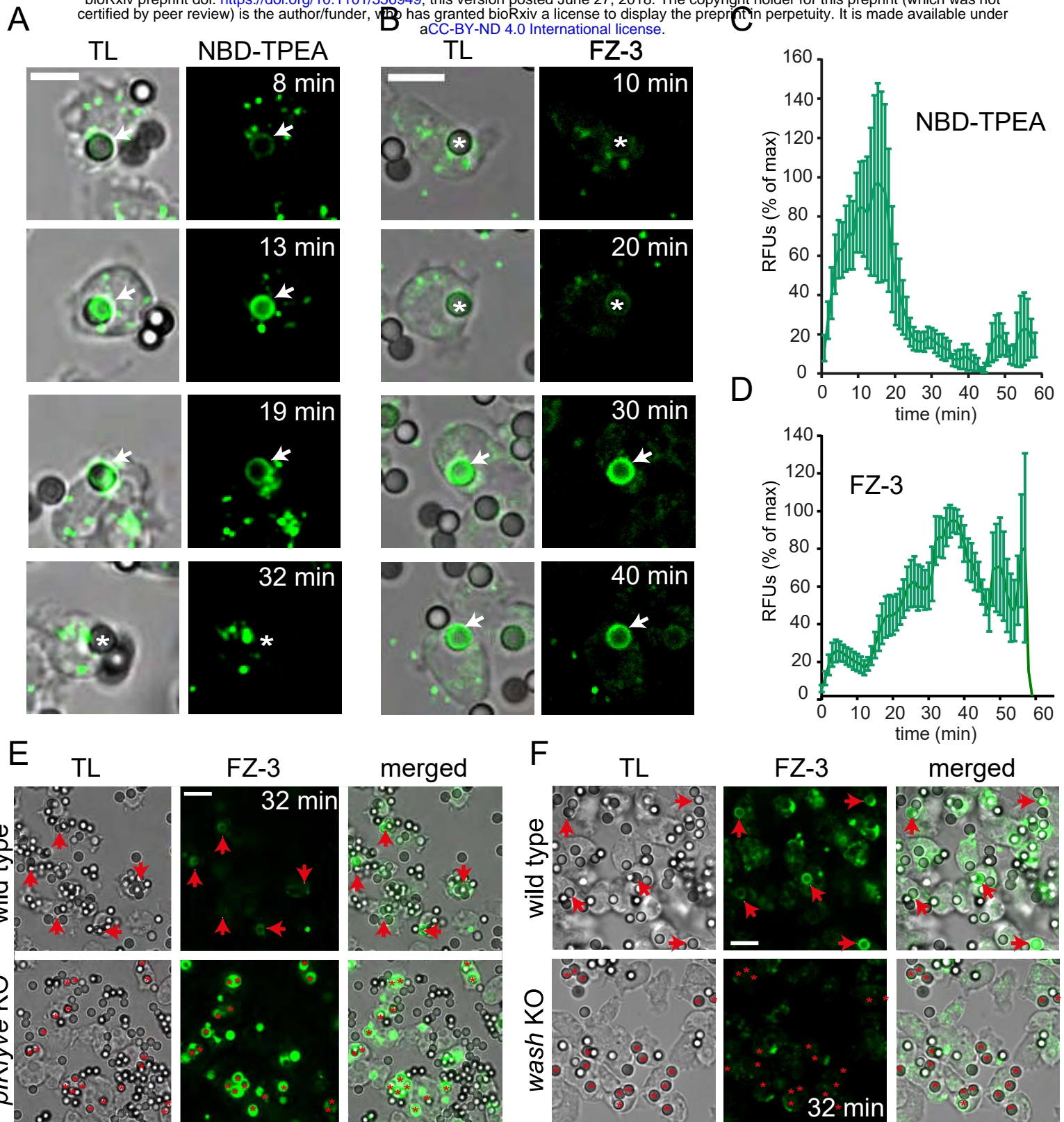
# Barisch *et al.*, Figure 1





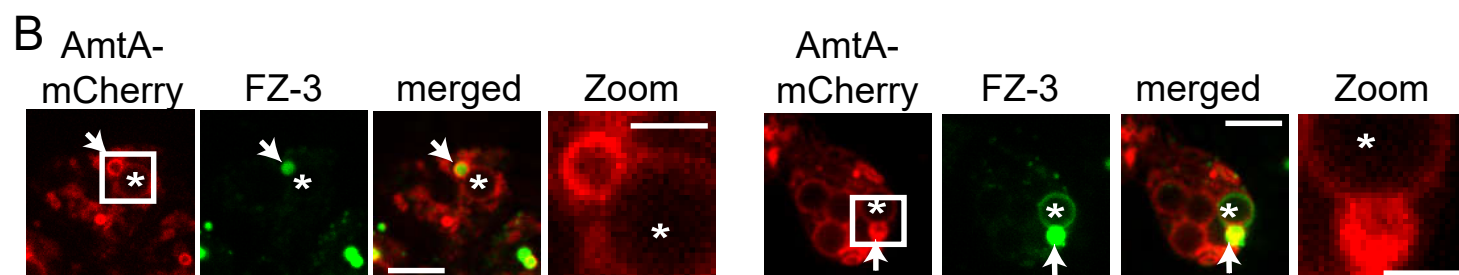
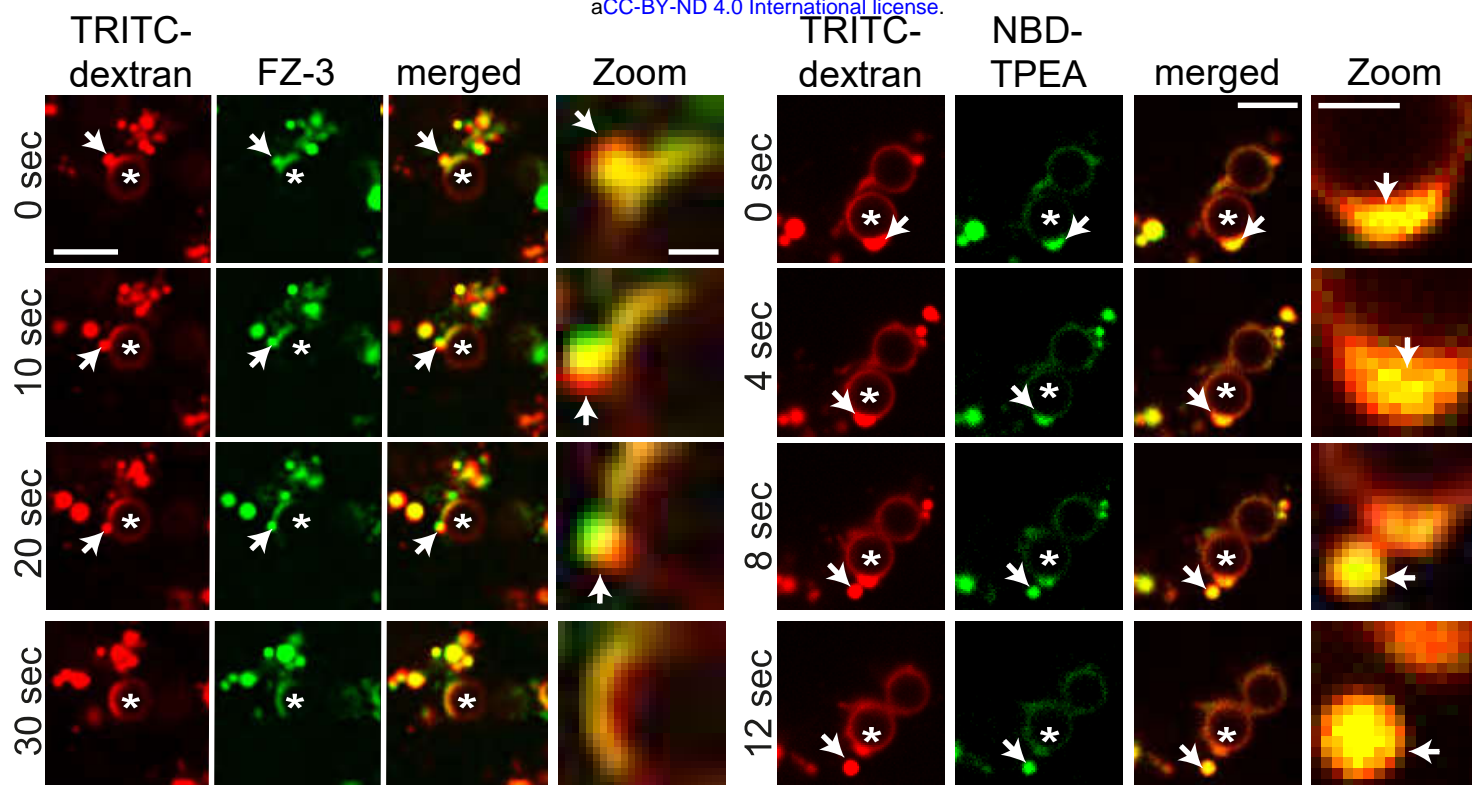
# Barisch *et al.*, Figure 2

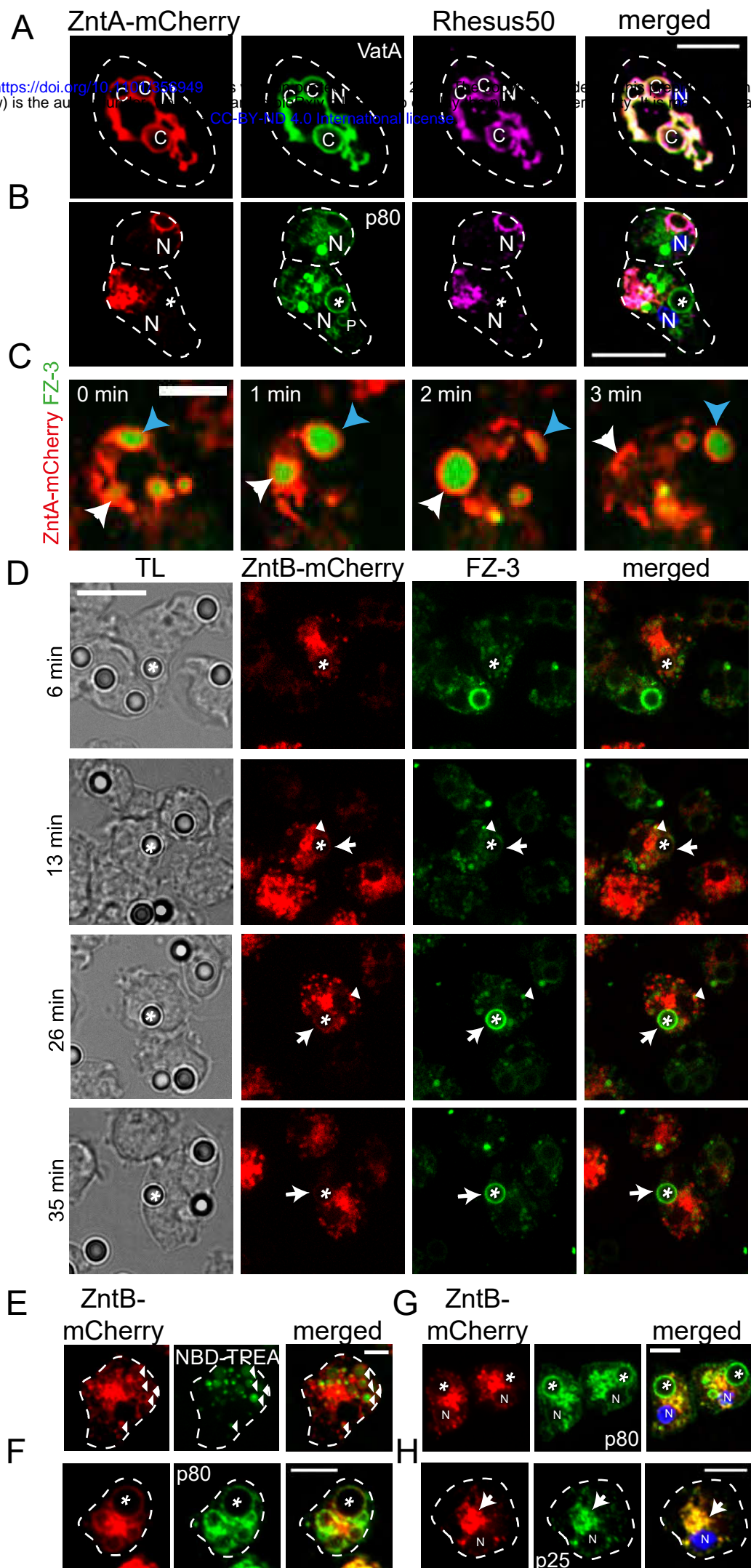
bioRxiv preprint doi: <https://doi.org/10.1101/356949>; this version posted June 27, 2018. The copyright holder for this preprint (which was not certified by peer review) is the author/funder, who has granted bioRxiv a license to display the preprint in perpetuity. It is made available under aCC-BY-ND 4.0 International license.



# Barisch *et al.*, Figure 3

**A** bioRxiv preprint doi: <https://doi.org/10.1101/356949>; this version posted June 27, 2018. The copyright holder for this preprint (which was not certified by peer review) is the author/funder, who has granted bioRxiv a license to display the preprint in perpetuity. It is made available under aCC-BY-ND 4.0 International license.



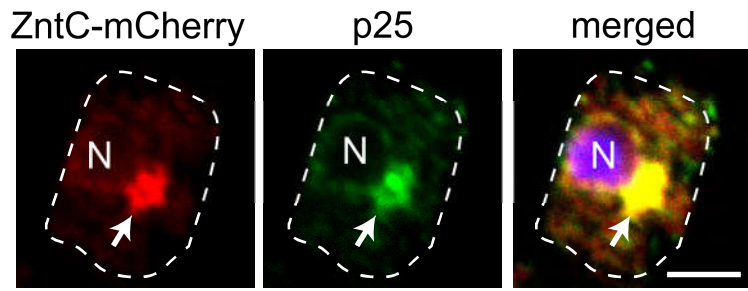




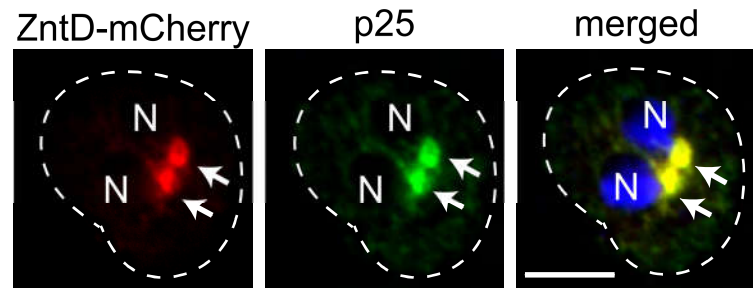
# Barisch *et al.*, Figure 5

bioRxiv preprint doi: <https://doi.org/10.1101/356949>; this version posted June 27, 2018. The copyright holder for this preprint (which was not certified by peer review) is the author/funder, who has granted bioRxiv a license to display the preprint in perpetuity. It is made available under aCC-BY-ND 4.0 International license.

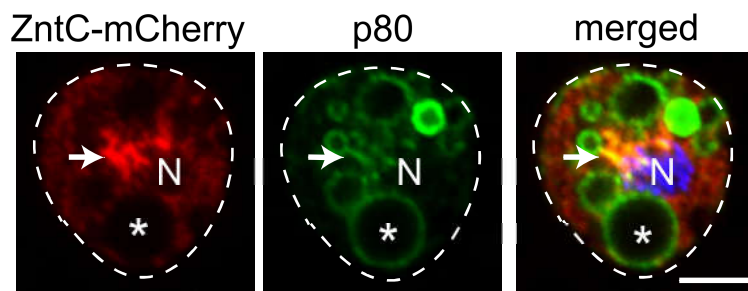
**A**



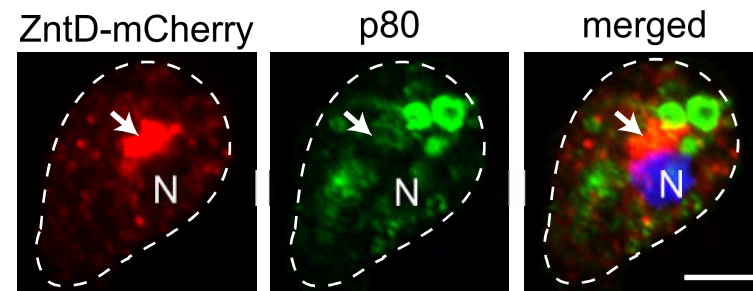
**B**



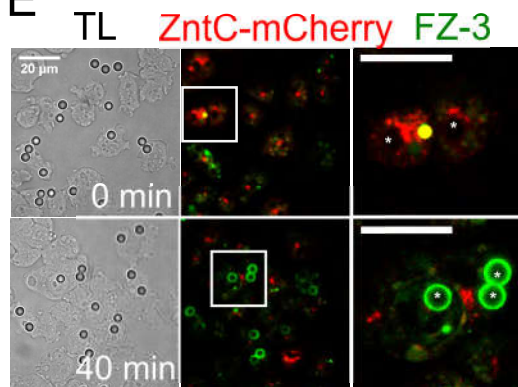
**C**



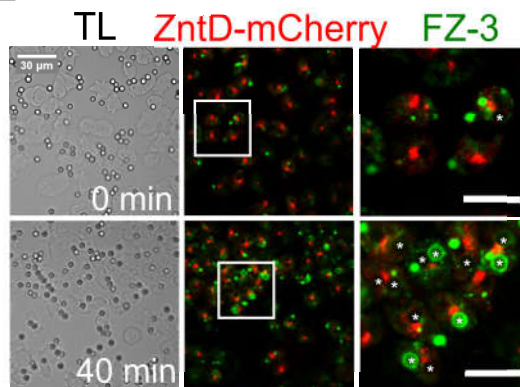
**D**



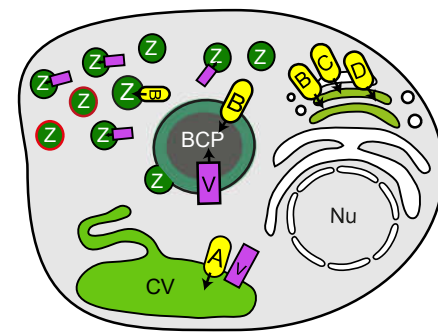
**E**



**F**

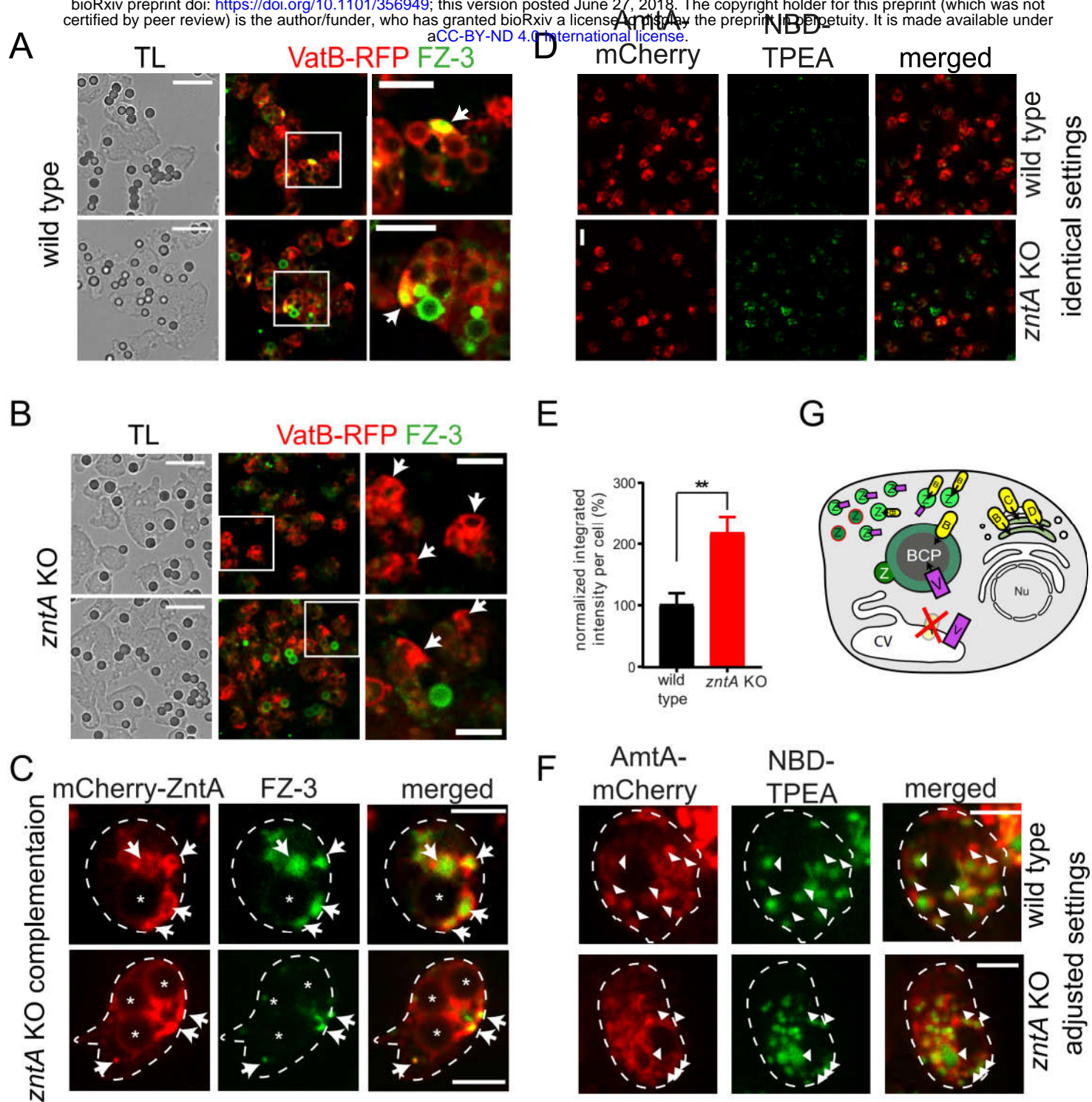


**G**

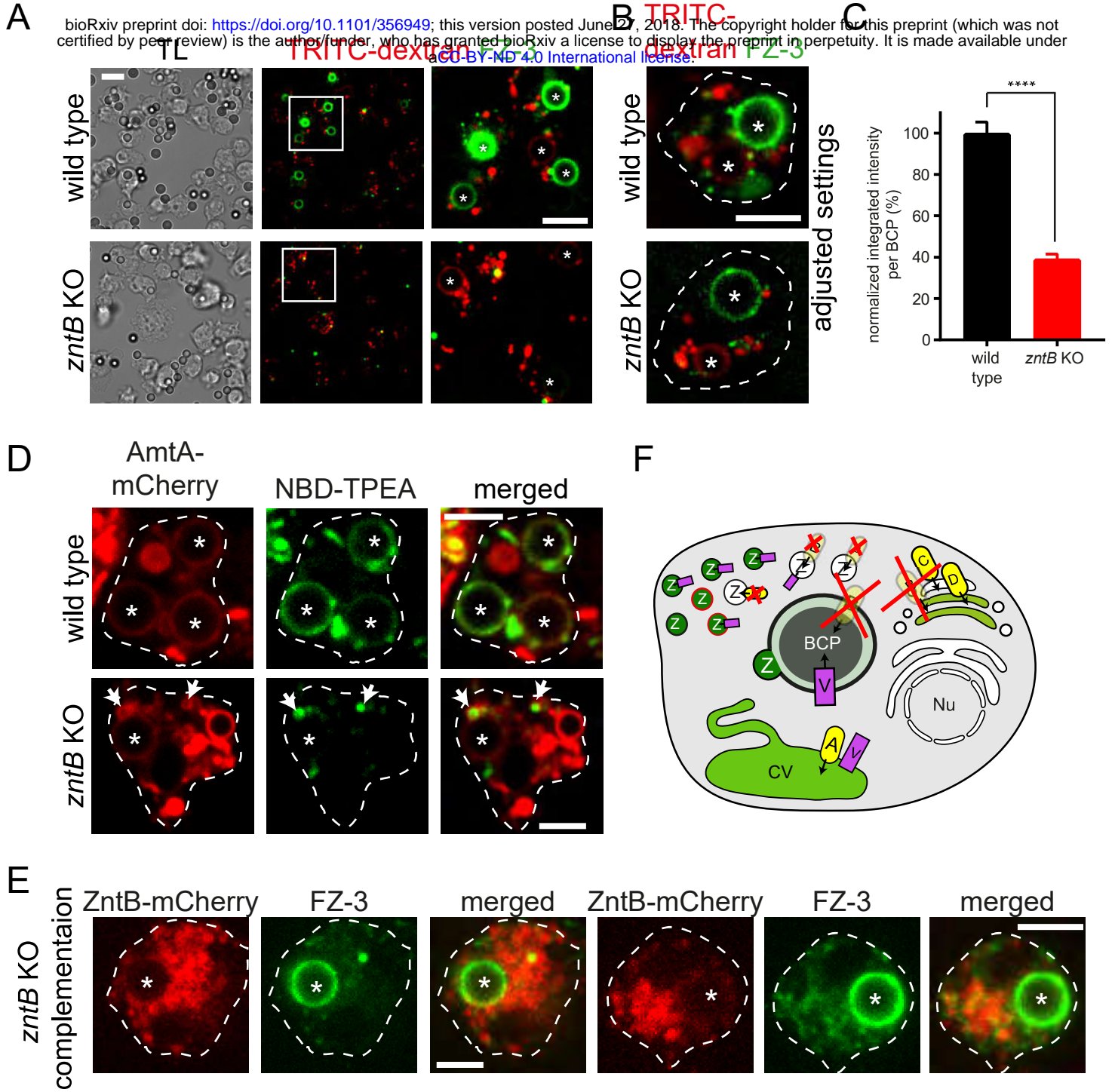


# Barisch *et al.*, Figure 6

bioRxiv preprint doi: <https://doi.org/10.1101/356949>; this version posted June 27, 2018. The copyright holder for this preprint (which was not certified by peer review) is the author/funder, who has granted bioRxiv a license to display the preprint in perpetuity. It is made available under aCC-BY-ND 4.0 International license.



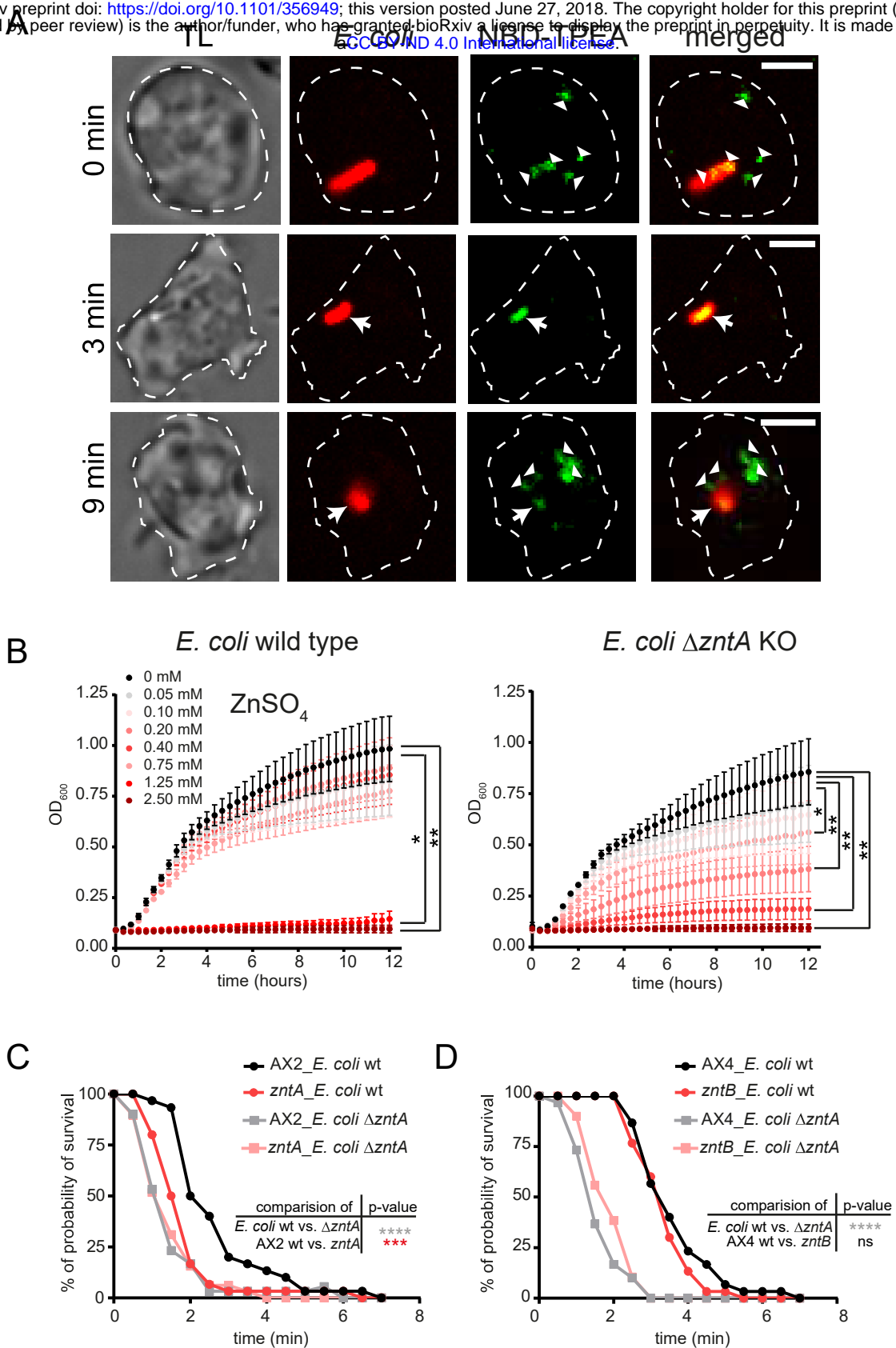
# Barisch *et al.*, Figure 7





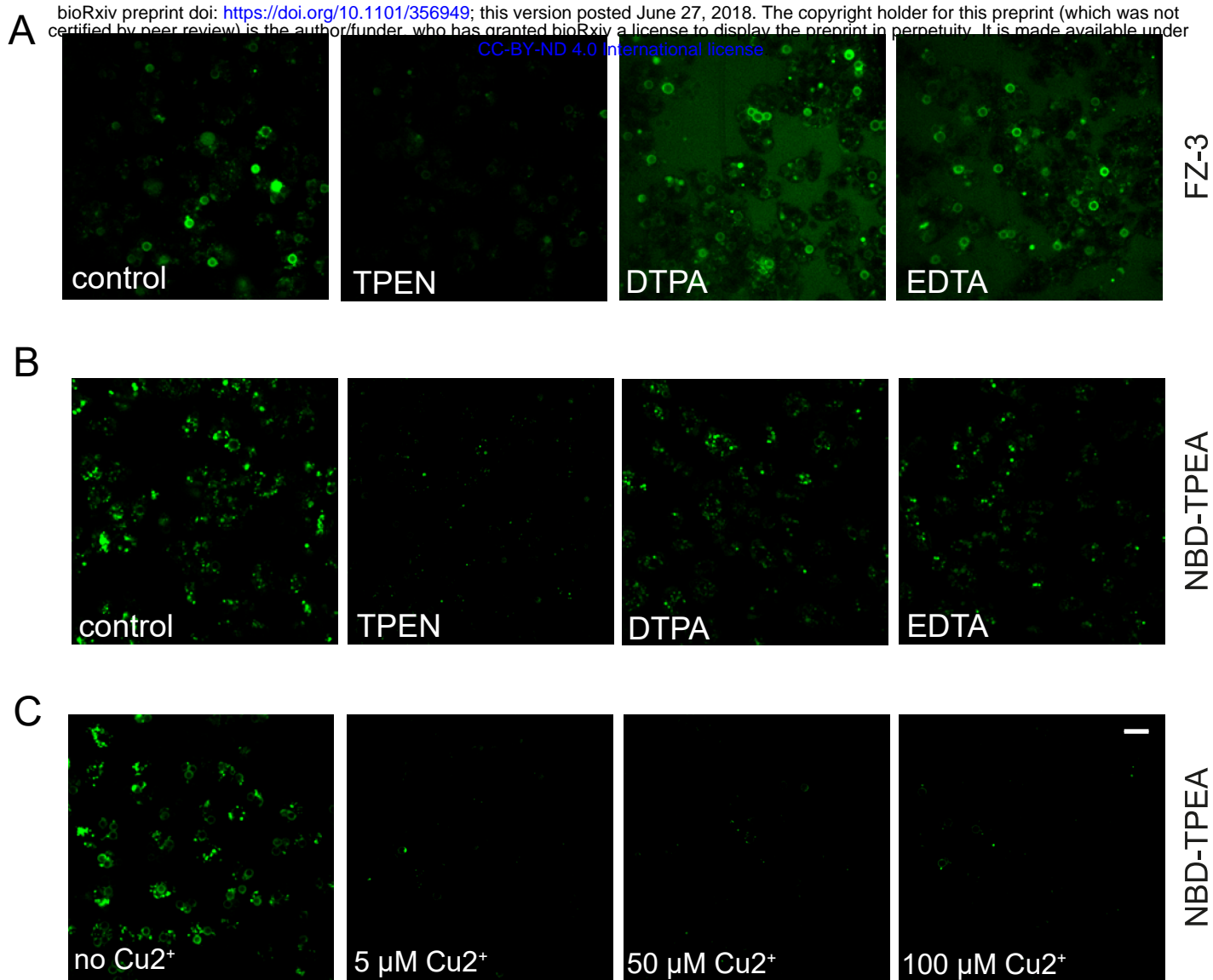
# Barisch *et al.*, Figure 8

bioRxiv preprint doi: <https://doi.org/10.1101/356949>; this version posted June 27, 2018. The copyright holder for this preprint (which was not certified by peer review) is the author/funder, who has granted bioRxiv a license to display the preprint in perpetuity. It is made available under aCC-BY-ND 4.0 International license.



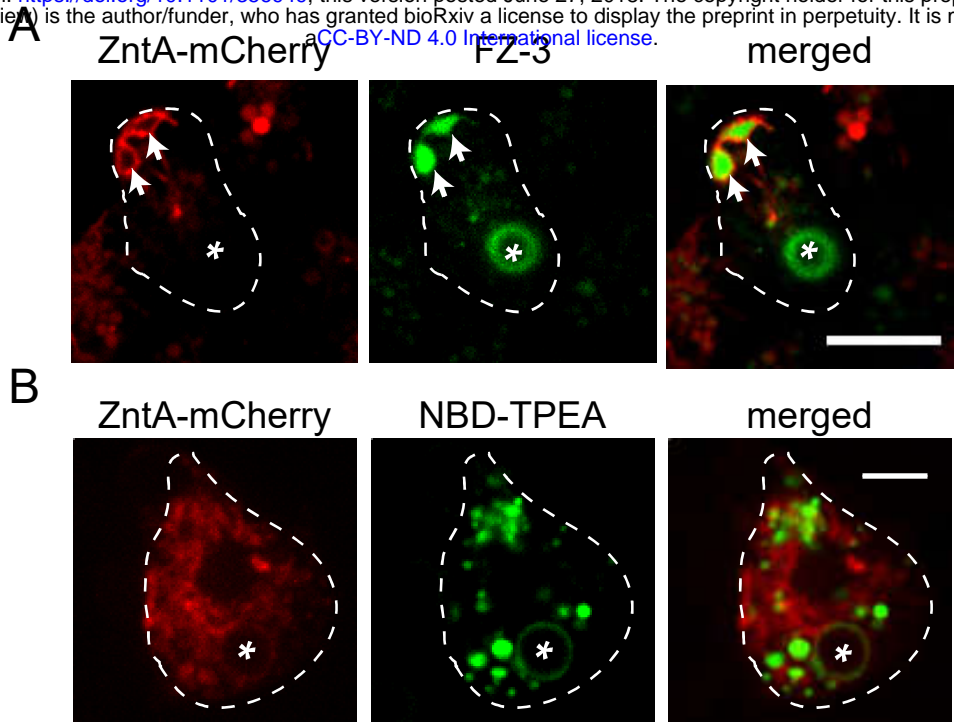
# Barisch *et al.*, Figure S1

A bioRxiv preprint doi: <https://doi.org/10.1101/356949>; this version posted June 27, 2018. The copyright holder for this preprint (which was not certified by peer review) is the author/funder, who has granted bioRxiv a license to display the preprint in perpetuity. It is made available under aCC-BY-ND 4.0 International license.



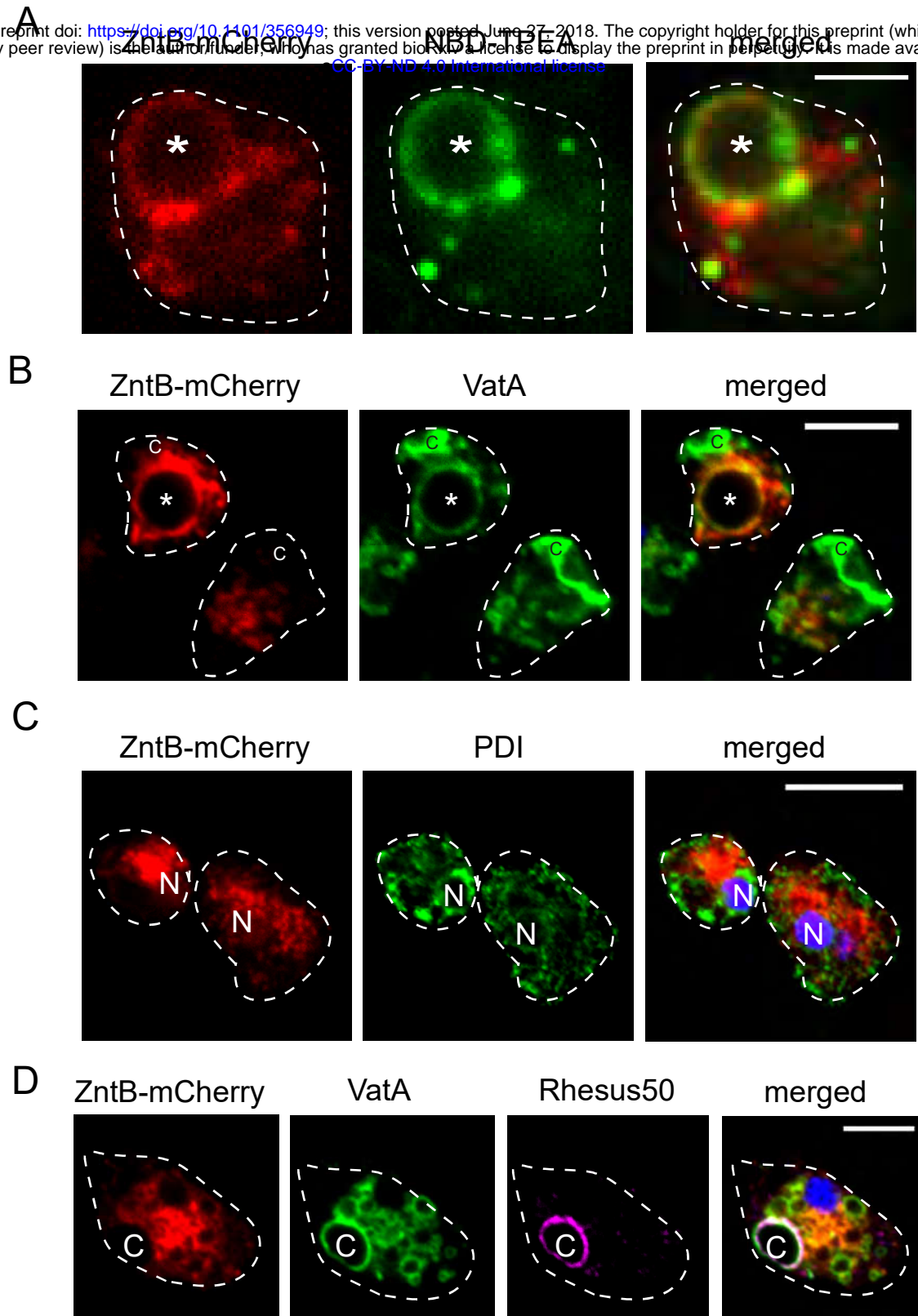
Barisch *et al.*, Figure S2

bioRxiv preprint doi: <https://doi.org/10.1101/356949>; this version posted June 27, 2018. The copyright holder for this preprint (which was not certified by peer review) is the author/funder, who has granted bioRxiv a license to display the preprint in perpetuity. It is made available under aCC-BY-ND 4.0 International license.



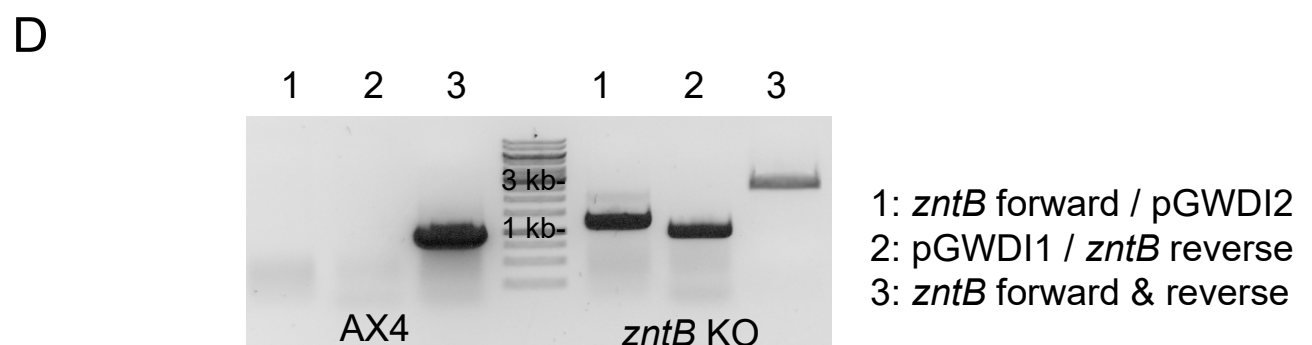
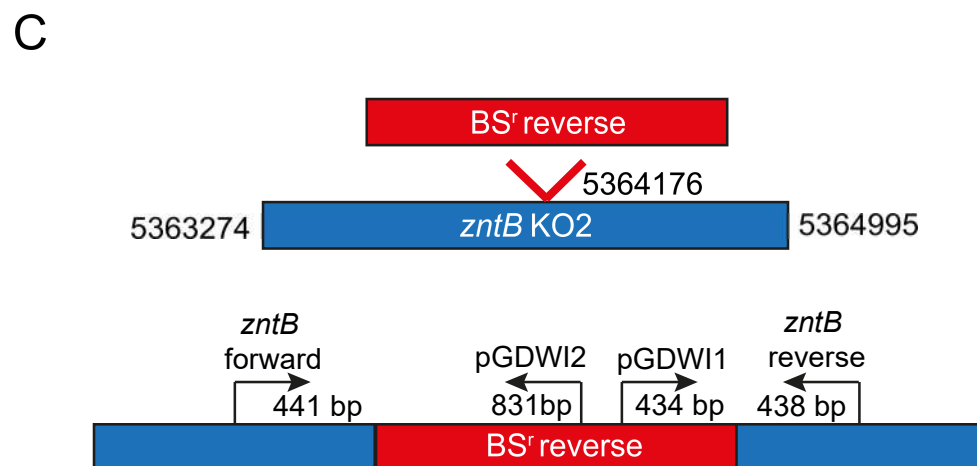
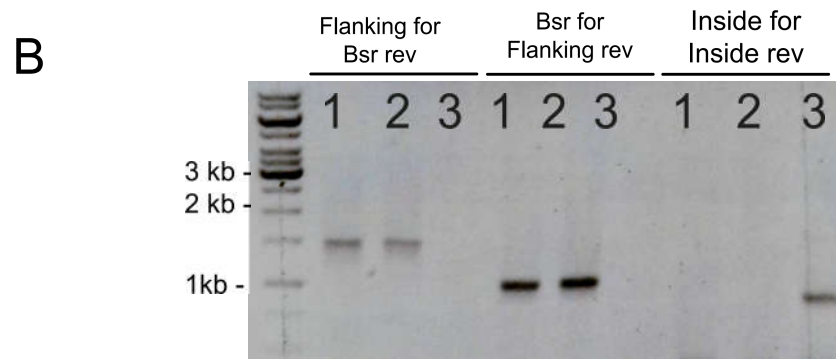
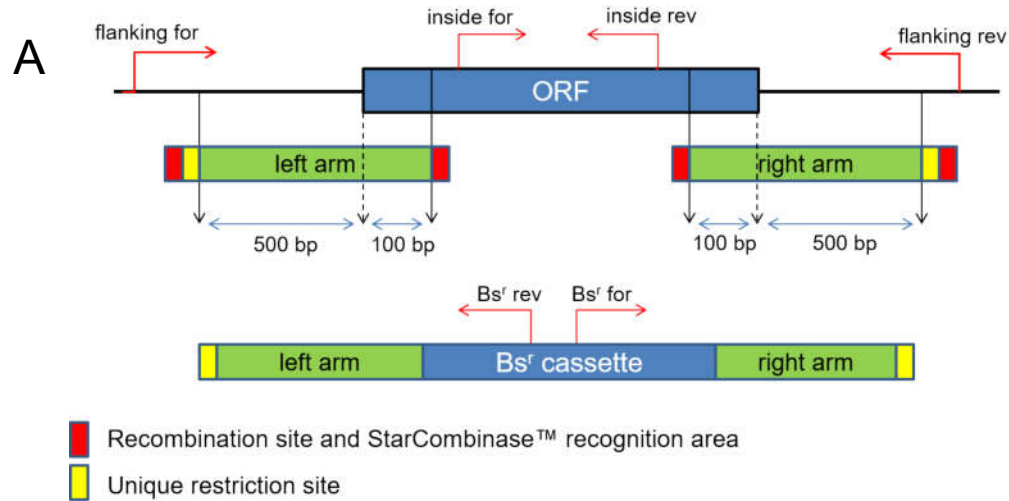
# Barisch *et al.*, Figure S3

A bioRxiv preprint doi: <https://doi.org/10.1101/356949>; this version posted June 27, 2018. The copyright holder for this preprint (which was not certified by peer review) is the author/funder, who has granted bioRxiv a license to display the preprint in perpetuity. It is made available under aCC-BY-ND 4.0 International license.



# Barisch *et al.*, Figure S4

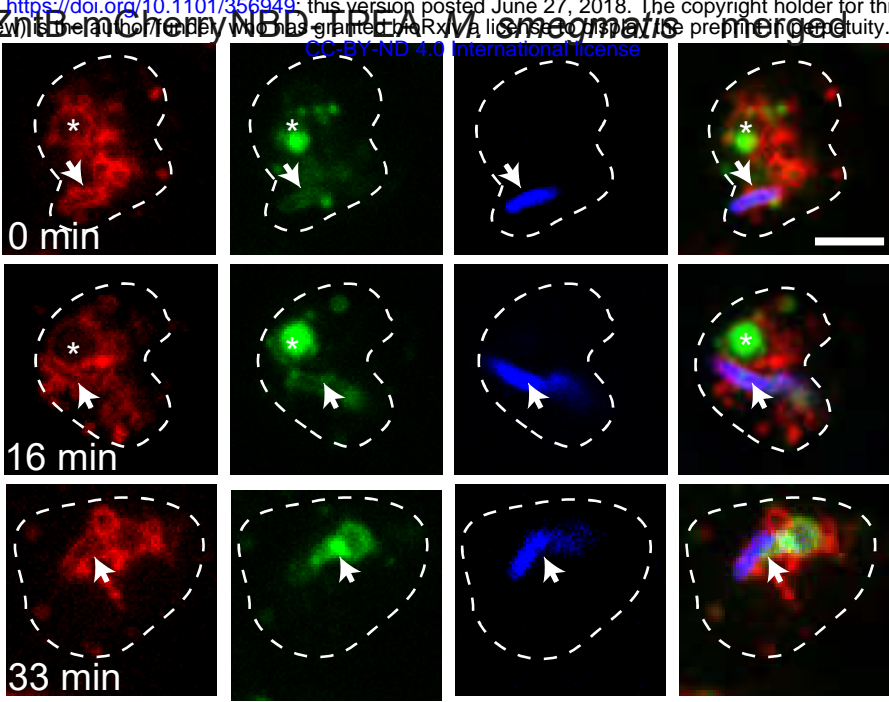
bioRxiv preprint doi: <https://doi.org/10.1101/356949>; this version posted June 27, 2018. The copyright holder for this preprint (which was not certified by peer review) is the author/funder, who has granted bioRxiv a license to display the preprint in perpetuity. It is made available under aCC-BY-ND 4.0 International license.





# Barisch *et al.*, Figure S5

bioRxiv preprint doi: <https://doi.org/10.1101/356949>; this version posted June 27, 2018. The copyright holder for this preprint (which was not certified by peer review) is the author/funder, who has granted bioRxiv a license to display the preprint in perpetuity. It is made available under aCC-BY-ND 4.0 International license.



# Barisch *et al.*, Figure S6

bioRxiv preprint doi: <https://doi.org/10.1101/356949>; this version posted June 27, 2018. The copyright holder for this preprint (which was not certified by peer review) is the author/funder, who has granted bioRxiv a license to display the preprint in perpetuity. It is made available under aCC-BY-ND 4.0 International license.

